A multi-dimensional stability model for predicting shallow landslide size and shape across landscapes

David G. Milledge[1], Dino Bellugi[2], Jim McKean[3], Alexander L. Densmore[1], William E. Dietrich[4]

1 Department of Geography, Durham University.

2 Department of Earth Atmospheric and Planetary Science, Massachusetts Institute of Technology,

3 U.S. Department of Agriculture, Forest Service, Rocky Mountain Research Station, Boise, Idaho

4 Department of Earth and Planetary Science, University of California, Berkeley

Corresponding author: David Milledge, Department of Geography, Durham University, Science Laboratories, South Road, Durham, DH1 1JJ, UK. (d.g.milledge@durham.ac.uk)

Key points

We derive a multi-dimensional stability model appropriate for natural landscapes

In all soils there is a critical depth and a minimum size for shallow landslides

The model provides a mechanistic explanation for observed depth-area scaling

Abstract

The size of a shallow landslide is a fundamental control on both its hazard and geomorphic importance. Existing models are either unable to predict landslide size or are computationally intensive such that they cannot practically be applied across landscapes. We derive a model appropriate for natural slopes that is capable of predicting shallow landslide size but simple enough to be applied over entire watersheds. It accounts for lateral resistance by representing the forces acting on each margin of potential landslides using earth pressure theory, and by representing root reinforcement as an exponential function of soil depth. We test our model's ability to predict failure of an observed landslide where the relevant parameters are well constrained by field data. The model predicts failure for the observed scar geometry and finds that larger or smaller conformal shapes are more stable. Numerical experiments demonstrate that friction on the boundaries of a potential landslide increases considerably the magnitude of lateral reinforcement, relative to

27 that due to root cohesion alone. We find that there is a critical depth in both cohesive and cohesionless soils,

28 resulting in a minimum size for failure, which is consistent with observed size frequency distributions.

29 Furthermore, the differential resistance on the boundaries of a potential landslide is responsible for a critical

30 landslide shape which is longer than it is wide, consistent with observed aspect ratios. Finally, our results

31 show that minimum size increases as approximately the square of failure surface depth, consistent with

32 observed landslide depth-area data.

Index terms

34 Geomorphology: hillslope; Debris flow and landslides; Mathematical and computer modeling;

Key words

36 shallow landslides; landslide size; depth-area scaling; slope stability model

1. Introduction

38 Shallow landslides usually involve only the colluvial soil mantle, and are generally translational,

39 failing along a quasi-planar surface. They are important as agents of landscape-scale sediment transfer and

40 erosion as well as potential hazards to life and infrastructure [Spiker and Gori, 2003]. The importance of

41 each landslide is defined by its, location and size.

42 While much progress has been made in mechanistic prediction of landslide location [e.g. Montgomery

43 and Dietrich, 1994; Casadei *et al.*, 2003a; Tarolli and Tarboton, 2006; Baum *et al.* 2010; Lanni *et al.*, 2012]

44 we remain limited in our understanding of what controls landslide size (area and depth), which is

45 fundamental to both hazard [Hungr *et al.*, 2008], and geomorphic change [Dietrich *et al.,* 2008]. Field

46 mapped inventories of shallow landslides (Figure 1; Rice *et al.* [1969]; Montgomery [1991]; Morgan *et al.*

47 [1997]; Gabet and Dunne [2002]; Paudel *et al.* [2003]; Warburton *et al.* [2008]; Larsen et al. [2010]) show

48 that their scar size varies across several orders of magnitude in volume (10^0-10^5 m^3) and area (10^1-10^4 m^2).

49 All six inventories have clear modes (Figure 1a) and 70% of the scar areas are between 30 and 300 m^2. The

50 landslides are generally longer than they are wide (Figure 1b; L>W for 70-100% of landslides), and wider

51 than they are deep (W>D for 99% of landslides). Since the landslides are generally restricted to the soil

52 mantle they rarely extend beyond a few meters deep, and the majority are between 0.1 and 1 m deep (Figure

53 1c). Landslide depth appears to scale as a power function of surface area both for some individual

54 inventories (Figure 1d) and for global compilations of soil and bedrock landslides, albeit with almost two

55 orders of magnitude of scatter in the global compilation [Guzzetti *et al.*, 2009; Larsen *et al.*, 2010].

56   Why do shallow landslide depth and area distributions have these characteristics, and why does

57 landslide depth scale with area? Why are landslides longer than they are wide and wider than they are deep?

58   An absolute upper limit to size is defined by hillslope length and width, which limit the area of the

59 soil mantle that can fail as a single body [Frattini and Crosta, 2013]. In practice the upper limit is

60 considerably smaller and is likely to relate to the spatial extent of low-strength areas [Pelletier *et al.*, 1997;

61 Frattini and Crosta, 2013; Alvioli et al., 2014]. Soil thickness sets an upper limit on shallow landslide depth,

62 and most shallow landslides fail at the base of the colluvial soil where typically the permeability decreases

63 and strength increases [Larsen *et al.* 2010]. There is a theoretical lower limit to both landslide depth and area

64 in cohesive material because a landslide must be large enough for its driving force to overcome the constant

65 stress-independent cohesion on its failure surface. This has been demonstrated for a range of depth-varying

66 cohesion fields representative of soil and rock [Frattini and Crosta, 2013]; as well as root cohesion, which

67 dominates in many colluvial soils [Reneau and Dietrich, 1987; Casadei *et al.*, 2003b; Gabet and Dunne,

68 2002; Dietrich et al., 2008].

69   Between these limits to landslide depth, Dietrich *et al.* [2008] and Frattini and Crosta [2013] have

70 shown that frictional resistance and cohesion on the margins of a landslide interact to create a least stable

71 depth that can be within rather than at the base of the soil profile. Distributions of scar area have been

72 explained by: the dynamics of rupture propagation [Piegari et al., 2006; Stark and Guzzetti, 2009; Lehman

73 and Or, 2012] or the distribution of low strength patches [Pelletier *et al.*, 1997; Katz and Aharonov, 2006;

74 Frattini and Crosta, 2013; Alvioli et al., 2014 The presence of cohesion is essential to almost all these

75 explanations; in its absence, the controls on the lower limit to landslide depth and area have not been

76 identified.

77   Klar et al. [2011] used a two-dimensional analytical model to give the first mechanistic explanation for

78 the observed scaling relationship between landslide depth and area (Figure 1d). Applying the model to

79   slopes of varying length they found that depth scaled as approximately the square root of landslide length,

80   where landslide length is defined by slope length and depth is the free parameter. This can be used to

81   reproduce the square root dependence of landslide depth on area under the following assumptions: 1) that

82   landslide width is a linear function of length; and 2) that either landslide length is always constrained and

83   depth the free parameter or the modelled length-depth relationship can be inverted to predict length when

84   depth is constrained and length the free parameter [Klar et al., 2011].

85   Observed landslide length and width almost always exceed depth, with depths generally less than 2 m

86   and areas greater than 4 m^2 [Larsen et al., 2010]. It is commonly acknowledged that length exceeds width

87   [e.g., Gabet and Dunne, 2002; Rickli, *et al.*, 2008; Marchesini *et al.*, 2008]. However, very few studies have

88   attempted to explain this behavior. Lehman and Or [2012] were able to reproduce, but not explain, the

89   general behavior of length and width using a fiber bundle model to represent progressive failure, but

90   suggested that their results were strongly dependent on model choices as well as local heterogeneities.

91   We aim: 1) to examine whether resistances on the margins of a landslide influence its length and

92   width; 2) to extend the existing theory on lower limits to landslide depth and area from cohesive soils into

93   cohesionless soils; and 3) to develop an alternative physically-based explanation for the observed landslide

94   depth-area scaling. To do this we need a slope stability model that can test the stability of potential

95   landslides of varying three-dimensional geometries with different material properties and that is suitable for

96   application to natural slopes. Since none of the currently available stability models fully satisfy these

97   requirements (see review in Section 2), we derive a new model that retains the low data requirements of

98   existing models but is more faithful to the key processes that control the stability of natural slopes (Section

99   3). We demonstrate the implications of the new analysis in Section 4 then test it for an observed landslide

100   where the parameters are well constrained by field measurement (Section 5). Finally, we apply the model to

101   identify the physical mechanisms that explain the observations above.

2. Existing slope stability models

103   Most slope stability models perform a limit-equilibrium analysis for a defined failure surface,

104   assuming that stresses are uniformly mobilized over the whole failure surface, and that the soil mass behaves

105   as one or more rigid blocks. Shallow landslide models almost exclusively use the simplest form of this

106   analysis: the one-dimensional infinite slope equation [Haefeli, 1948; Taylor, 1948; Skempton and de Lory,

107   1957] coupled with a hydrological model to estimate the local pore pressure field [e.g. Montgomery &

108   Dietrich 1994; Iverson 2000; Casadei *et al.*, 2003a; Tarolli and Tarboton, 2006; Baum *et al.*, 2008; Lanni *et*

109   *al.* 2012]. However, understanding landslide size and shape requires a three-dimensional model where the

110   dimensions of the landslide can be examined explicitly and where the resistance on the margins of a

111   potential landslide can be represented.

112   The simplest three-dimensional approaches consider the forces acting on a single block in limiting

113   equilibrium and treat either lateral root reinforcement [Burroughs, 1985; Reneau and Dietrich, 1987;

114   Montgomery *et al.*, 2000; Gabet and Dunne, 2002; Casadei *et al.*, 2003b] and/or boundary pressure on the

115   margins of the block [Chen, 1981; Burroughs, 1985]. When included, root reinforcement is generally treated

116   as an effective cohesion. Boundary pressures are modeled using earth pressure theory and assuming an

117   active wedge upslope of the block (driving failure), a passive wedge downslope (resisting failure), and

118   pressure on the cross-slope sides generating shear resistance due to friction. With the exception of

119   Burroughs [1985], the upslope and downslope wedges were assumed to be horizontal (i.e. earth pressure

120   coefficients depended only on soil friction angle). Furthermore, cohesion is either ignored or represented as

121   an additive term on the upslope and downslope boundaries, rather than acting on the wedges themselves.

122   This is particularly problematic in the downslope case where the soil is failing under compression.

123   An alternative approach is to extend the two-dimensional method of slices [e.g. Morgernstern and

124   Price, 1967; Spencer, 1967] into the third dimension, discretizing the landscape into columns [e.g. Hovland,

125   1977; Lam and Fredlund, 1993]. However, these methods do not consider shear resistance (due to friction or

126   cohesion) on the cross-slope boundary between stable and unstable columns and so underestimate shear

127   resistance on that boundary [Stark and Eid, 1998; Chugh, 2003].

128   Dietrich *et al.* [2008] applied a framework similar to Hovland's [1977] method, but parameterized the

129   forces on the margins of the landslide using methods similar to Burroughs [1985]. Dietrich *et al.* [2008]

130   assumed horizontal upslope and downslope wedges to enable an analytical solution but inclined the resultant

131   forces by the soil friction angle to represent friction on the margin between the blocks. As in Burroughs

132   [1985] they assumed that the upslope and downslope wedges are cohesionless, and then added cohesion to

133   each of the block's vertical boundaries.

134   In a limit equilibrium analysis, all forces are assumed to occur at the same instant. However, some

135 slides may develop incrementally with a small area failing first and its load then being transferred to

136 neighboring areas, causing them to fail. This style of progressive failure is normally modeled using a Finite

137 Element Model [Duncan, 1996; Griffiths and Marquez, 2007], but Lehmann and Or [2012] attempted to

138 approximate progressive failure in a limit equilibrium framework by treating deformation implicitly using

139 rigid columns, but removing and re-distributing the load of each column once it had failed by basal shear.

140 They represented the driving and resisting forces acting on the basal, upslope, downslope, and cross-slope

141 margins of each column, focusing on cohesive effects. They did not represent friction on the cross-slope

142 margin and an upslope cell only exerts a driving force on its downslope neighbors once it has failed at its

143 base. They represented the critical downslope stress required to cause failure using a water-dependent

144 compression strength threshold [Mullins and Panayiotopoulos, 1984] that does not account for the self-

145 weight of the soil, which is appropriate for unconfined samples but not for natural slopes.

146   These models have enabled analysis of discrete landslides within a limit equilibrium framework and

147 are capable of representing the lateral forces acting on a potential landslide, which is essential for a three-

148 dimensional treatment. However, they are generally limited by their treatment of upslope and downslope

149 margins, either assuming that the ground surface is horizontal above and below the landslide, incorrectly

150 accounting for cohesion on these margins or neglecting the self-weight of the soil. This is a problem because

151 the forces acting on these margins can strongly affect both the stability of the slope and the geometry of the

152 landslide. To address this problem, we extend the method presented by Dietrich *et al.* [2008]; relaxing the

153 assumption that the upslope and downslope wedges have a horizontal surface, and include the effect of

154 cohesion on their failure surface (i.e. earth pressure coefficients depend on friction angle, slope, and

155 cohesion). This approach retains the simplicity and analytical tractability of standard limit equilibrium

156 approaches but is a more faithful representation of natural slope conditions.

157 **3. The multi-dimensional shallow landslide model (MD-STAB)**

158   The MD-STAB model satisfies horizontal and vertical force equilibrium while ignoring moment

159 equilibrium. A shallow landslide is represented by three connected three-dimensional hillslope segments: an

160 active (upslope) wedge, a central block and a passive (downslope) wedge. A force balance is calculated on

161 the central block. Figure 2 shows the geometry of the three segments and force polygons which illustrate the

162 magnitude and orientation of the forces acting on the central block. The central block is assumed to be rigid

163 and to fail by shear on a plane parallel to the ground surface at a prescribed depth. Typically this plane is the

164 soil-bedrock interface, which is often the location of the largest contrast in material strength in hillslope

165 soils. We also explore the influence of failure plane depth on the stability and size of a potential landslide.

166 We assume that failure occurs in drained conditions and that groundwater flow is steady and parallel to the

167 slope surface, although other groundwater assumptions could also be used to predict a pore water pressure

168 field. We also ignore any infiltration, suction or capillary rise effects in an unsaturated zone, and simply

169 partition the landslide block into saturated and unsaturated zones. This allows definition of a saturation ratio

170 ($m=h/z$) where h is the height of the water table and z is the depth to the failure surface. Driving forces

171 include the downslope component of the central block mass plus the force on the central block from the

172 upslope wedge where active earth pressure conditions are assumed. Resisting forces are considered on all

173 boundaries of the central block, and include the passive earth pressure from the downslope wedge and soil

174 friction and root cohesion on the base, cross-slope, upslope and downslope sides. Cohesion is not directly

175 added at the upslope and downslope vertical boundaries of the central block. Instead, resistance due to

176 cohesion is incorporated in the passive and active wedges themselves and affects the corresponding earth

177 pressures that those wedges impose on their boundaries with the central slide block. The following sections

178 describe in detail the conceptualization of the driving and resisting forces internal and external to the central

179 slide block, and how the forces are combined to evaluate the factor of safety of a potential landslide.

180 ### 3.1. Central block driving force (F_{dc})

181   This model component represents the driving force caused by the mass of the slide block itself. We

182 follow closely the standard formulation used in other plane strain landslide analyses, such as a method of

183 slices or the infinite slope method, but eventually calculate a driving force, rather than stress, for a finite

184 three-dimensional slide (Figure 2a). The total vertical geostatic stress σ_z at depth z caused by the soil above

185 it is:

$$\sigma_z = \gamma_s\, z \qquad\qquad (1)$$

186 where γ_s is the unit weight of the soil ($\gamma_s = g\,\rho_s$), ρ_s is the constant bulk density of soil and g is gravitational

187 acceleration. Note that in common with many other studies [e.g. Montgomery and Dietrich, 1994; Iverson,

188 2000; Gabet and Dunne, 2002; Baum *et al.*, 2008; Lanni *et al.*, 2012] we assume a single soil density

189 independent of soil moisture content since it ultimately has very little impact on the computed factor of

190 safety. The driving component of this stress τ acts downslope along the failure surface and is:

$$\tau = \sigma_z \sin\theta\cos\theta = \gamma_s\, z\sin\theta\cos\theta \qquad (2)$$

191 where θ is the slope inclination(Figure. 2). The corresponding driving force F_{dc} acting downslope along

192 the failure surface is the driving stress integrated over the planimetric length and width of the slide (polygon

193 P1 in Figure 2c):

$$F_{dc} = \gamma_s z\, wl \sin\theta\cos\theta \qquad (3)$$

194 where: l is the slide length and w is its width (Figure 2).

3.2. Block cross-slope boundaries (F_{rl})

196 Shear resistance on the two parallel and vertical cross-slope sides of the slide block F_{rl} results from

197 friction and cohesion. These sides are the surfaces ABB'A' and DCC'D' in Figure 2a, and the forces acting

198 on them are shown by polygons P5 and P6 in Figure 2d. Following Stark and Eid [1998], we represent

199 friction by assuming that external horizontal and vertical forces act at the centers of the two sides and that

200 these forces can be predicted from standard earth pressure theory. For a homogeneous soil with isotropic

201 frictional properties, the shear resistance due to lateral earth pressure on the cross-slope sides is the product

202 of the horizontal stress at a point and the soil friction angle (polygons P5 and P6 in Figure 2d). We assume

203 that in the cross-slope direction, earth pressure in the soil layer is in an intermediate or "at-rest" condition

204 (i.e. it does not experience active or passive yield during failure). The at-rest lateral earth pressure σ'_x at any

205 point is conventionally calculated from the vertical effective pressure σ'_z as:

$$\sigma'_x = K_o\, \sigma'_z \qquad (4)$$

206 where K_0 is the coefficient of at-rest earth pressure. Since σ'_z increases linearly with depth, σ'_x has the

207 triangular stress distribution shown in Figure 2b. The at-rest earth pressure coefficient is poorly constrained

208 for soils with cohesion. In particular, when roots contribute to this cohesion they may support some of the

209   vertical geostatic stress reducing the value of K_0, but this effect is difficult to quantify. As a result, most

210   applications use Jaky's [1944] empirical formula for cohesionless, normally consolidated soils, commonly

211   found on natural slopes [Das, 2009]. Under these assumptions the at-rest earth pressure coefficient is:

$$K_O = 1 - \sin\phi' \tag{5}$$

212   where ϕ' is the effective friction angle of the soil. The cross-slope resisting stress s_c on the vertical sides of

213   the slide block is:

$$s_c = K_o \, \sigma_z' \tan\phi' \tag{6}$$

214   To calculate the resisting force F_{rc} on a cross-slope boundary, we integrate Equation 6 over the cross-

215   slope area of the slide block, ($l \, z \, \cos\theta$) and add the depth averaged cohesion C'_{rl} acting over the same area

216   (polygons P5 and P6 in Figure 2d):

$$F_{rl} = \frac{1}{2} K_o (\gamma_s - \gamma_w m^2) l z^2 \cos^2\theta \tan\varphi' + C'_{rl} \, l \, z \cos\theta \tag{7}$$

217   where γ_w is the unit weight of water, m is the saturation ratio ($m=h/z$), and h is the height of the water table

218   above the failure surface.

219   3.3. Block upslope (F_{du}) and downslope (F_{rd}) boundaries

220   For a landslide to occur, i.e. for shear to develop on the base of the central block, the downslope

221   wedge must fail and mobilize under passive or compressive earth pressure conditions. At the same time, the

222   failing central block will move away from the soil upslope of it, creating active or tensile conditions in the

223   upslope wedge. We model the interfaces between these wedges and the central block as vertical boundaries

224   (see the surfaces BCC'B' and ADD'A' in Figure 2a). The effects of these two soil wedges on the central

225   block are calculated from the active F_a and passive F_p forces that they impose on these upslope and

226   downslope vertical boundaries (polygons P2 and P3, in Figure 2c). The active and passive forces are defined

227   using standard earth pressure theory (e.g. used to analyze retaining wall stability), but including cohesion in

228   the up/downslope wedges and an inclined soil layer appropriate for natural slopes.

229   Classical soil mechanics theory includes three primary methods of active and passive earth pressure

230   prediction, the Rankine, Coulomb and log-spiral methods, which are described in standard soil mechanics

231   textbooks [e.g., Das, 2009]. All three methods assume a homogeneous and isotropic soil. The Rankine

232   [1857] method is a lower-bound plasticity solution based on statically admissible stress fields, while the

233   Coulomb [1776] and log-spiral methods [Caquot and Kerisel, 1948; Chen, 1975] are upper-bound solutions

234   based on kinematically admissible velocity fields [Das, 2009]. The three methods have also been modified

235   to allow for a sloping soil layer and cohesive soil [Chugh and Smart, 1981; Mazindrani and Ganjali, 1997;

236   Gnanapragasam, 2000; Soubra and Macuh, 2002].

237   These earth pressure theories primarily differ in how they treat stress conditions on their boundaries

238   with the central block and how they model the failure surface beneath the wedges. During failure the

239   upslope block will tend to move vertically downward along the interface with the central block as they both

240   translate downslope. This introduces a downward shear along the upslope boundary of the central block that

241   reorients the resultant active force by some angle δ from horizontal (polygon P2 in Figure 2c). On the

242   downslope passive interface, shear develops in the opposite sense and again the passive force is reoriented

243   from horizontal (polygon P3 in Figure 2c). The Rankine method assumes that the force reorientations are

244   equal to the slope angle (i.e. $\delta = \theta$), while δ can take any value from 0 to ϕ' in the Coulomb and log-spiral

245   methods [Duncan and Mokwa, 2001]. The Rankine and Coulomb methods assume that the failure surfaces

246   beneath the active and passive wedges are planar, but theory and observation demonstrate that they are

247   curved [Terzaghi, 1943]. In the active case the curvature is small and a planar assumption causes little error

248   [Craig, 2004]. But in the passive case, a planar failure surface results in passive pressure predictions that are

249   much too large, particularly if $\delta > 0.4 \phi'$ [Duncan and Mokwa, 2001]. Terzaghi [1943] described a failure

250   surface that took the form of the arc of a logarithmic spiral and passive earth pressure predictions using this

251   wedge geometry were found to be more accurate over any value of δ [Soubra, 2000; Zhu and Quian, 2000].

252   However, this requires optimizing the two parameters that describe the failure surface for each combination

253   of slope, friction angle, cohesion, and soil thickness.

254   Because of the uncertainty in analytical predictions of the active and passive forces on the central

255   block, we calculate lower and upper bounds. To obtain a lower-bound estimate, we use the Rankine method

256   at both margins. To obtain an upper-bound estimate, we use the log-spiral method, which can allow for

257   curvature on the failure surface, at the downslope margin and the simpler Coulomb method at the upslope

258   margin, which is typically planar. Following Mazindrani and Ganjali [1997], the Rankine solution for

259   cohesive soils on a hillslope gives the lower-bound active, K_a and passive, K_p earth pressure coefficients:

$$K_p, K_a = \frac{1}{\cos^2 \phi'}\left(2\cos^2\theta + 2\left(\frac{C'_{rl}}{\gamma_s z}\right)\cos\phi'\sin\phi' \pm \left(4\cos^2\theta\left(\cos^2\theta - \cos^2\phi'\right) + 4\left(\frac{C'_{rl}}{\gamma_s z}\right)^2\cos^2\phi' + 8\left(\frac{C'_{rl}}{\gamma_s z}\right)\cos^2\theta\sin\phi'\cos\phi'\right)^{0.5}\right) - 1 \quad (8)$$

260 where ϕ' is the soil friction angle; θ is the slope angle; C'_{rl} is the depth averaged cohesion; γ_s is the soil unit

261 weight; z is the depth of the failure plane of the central block; and the negative and positive signs are for the

262 active and passive cases, respectively. Following Chugh and Smart [1981], the Coulomb active earth

263 pressure coefficient K_a for sloping cohesive soils is defined as:

$$K_a = \frac{\cos\beta\cos\theta\sin(\beta - \phi') - 2\left(\dfrac{C'_{rl}}{\gamma_s z}\right)\cos\theta\cos\phi'}{\cos(\beta - \delta - \phi')\sin(\beta - \theta)} \quad (9)$$

264 where β is the inclination from horizontal of a planar failure surface from the base of the central block to the

265 ground surface upslope. We solve Equation 9 numerically to find the most critical failure plane (for θ-1° $< \beta$

266 $< 89°$) which maximizes the active earth pressure coefficient [Chugh and Smart, 1981].

267   We use the version of the log-spiral method derived by Soubra and Macuh [2002] to provide an upper-

268 bound solution for the passive resistance of sloping cohesive soils downslope of a potential slide mass.

269 Soubra and Macuh [2002] employed a rotational logarithmic spiral failure surface on the basis that under

270 these conditions an energy balance is equivalent to moment equilibrium about the center of the logarithmic

271 spiral. The solution requires identification of the most critical log-spiral failure plane (i.e. minimizing

272 passive pressure), and yields:

$$K_p = K_{p\gamma} + 2K_{pc}\left(\frac{C'_{rl}}{\gamma_s z}\right) \quad (10)$$

273 where $K_{p\gamma}$ and K_{pc} are the friction and cohesion components of the passive earth pressure coefficient

274 respectively. The passive earth pressure coefficient is thus a function of slope, friction angle, cohesion, soil

275 unit weight, soil depth and two geometry parameters α_0 and α_1, which define the geometry of the

276 logarithmic-spiral failure surface (full equations provided in Appendix 1). Following Soubra and Macuh

277 [2002], we solve Equation 10 numerically using a generalized reduced gradient algorithm [Lasdon *et al.*,

278 1978] to find the log-spiral failure surface that minimizes the passive earth pressure coefficient.

279   By treating the upslope and downslope margins as analogous to the wall in an earth pressure retaining

280 wall problem the active σ_a and passive σ_p stresses on the upslope or downslope margin of the central block

281 can be calculated as the product of the vertical effective pressure (σ'_z) and the active or passive earth

282 pressure coefficients from Equation 8, 9, or 10. For the passive downslope margin:

$$\sigma_p = K_p z(\gamma_s - \gamma_w m) \tag{11}$$

283 To calculate the total passive force on the downslope margin (ADD'A' in Figure 2a) we integrate

284 Equation 11 over the downslope boundary of the block (wz) perpendicular to the direction of sliding. This

285 passive force F_p, is the resultant of both the normal and shear forces (due to friction) on the boundary

286 between the central block and the wedge and is inclined at the boundary friction angle δ. We assume that

287 $\delta = \theta$, in the lower-bound case and $\delta = \varphi'$ in the upper-bound case. As a result, the passive force needs to be

288 decomposed into its slope-parallel component, which acts as a resisting force F_{rd}:

$$F_{rd} = F_p \cos(\delta - \theta) = \frac{1}{2} K_p z^2 (\gamma_s - \gamma_w m^2) w \cos(\delta - \theta) \tag{12}$$

289 and a slope normal component F_{nd}, which modifies the normal force on the base of the central block

290 (polygon P3 in Figure 2c):

$$F_{nd} = \frac{1}{2} K_p z^2 (\gamma_s - \gamma_w m^2) w \sin(\delta - \theta) \tag{13}$$

291 The active stress σ_a on the upslope margin follows the same form as the passive stress and can be

292 calculated from Equation 11 by replacing the passive coefficient with an active earth pressure coefficient K_a

293 for sloping soils. The net driving force on the upslope margin F_{du} can then be calculated from Equation 12

294 making the same substitution (Figure 2c). For soils with a strong cohesive component the active earth

295 pressure coefficient, and therefore the net driving force on the upslope margin, is negative since the resisting

296 forces due to cohesion exceed the driving force of the upslope wedge. In this case the negative F_{du}

297 represents a net resisting force on the upslope margin of the central block. Note that cohesion on the wedge

298 failure surface is included within the active and passive earth pressure coefficients and does not need to be

299 applied to the vertical upslope or downslope boundaries (Equations 12-13). The slope normal component of

300 the active force F_{nu}, which modifies the normal force on the base of the central block, can be calculated from

301 Equation 13 by replacing the passive with the active earth pressure coefficient (P2 in Figure 2c).

302 Standard earth pressure methods use a hydrostatic analysis to calculate earth pressure on the upslope

303 and downslope boundaries of the unstable block [Das, 2009]. In reality slope parallel seepage will exert a

304 force on these boundaries increasing the driving force on the upslope boundary and reducing passive

305 resistance on the downslope boundary. However, to our knowledge, there is currently no suitable earth

306 pressure method that can account for seepage forces in the upslope active wedge and downslope passive

307 wedge. We discuss the impact of this simplification on our findings in Section 6.4.

308

309 3.4. Basal resistance force (F_{rb})

310 Resistance along the base of the slide block F_{rb} develops by a combination of cohesion C'_{rb} and

311 friction, the product of normal force on the failure surface and the tangent of the friction angle. The normal

312 force F_{nt} is the effective normal stress on the failure surface integrated over its area (thus accounting for pore

313 pressure). It includes the normal force due to the self-weight of the central block (F_{nc}, polygon P1 in Figure

314 2c), and the components of the upslope F_{nu} and downslope F_{nd} forces that act normal to the failure surface

315 (polygon P4 in Figure 2c):

$$F_{nt} = F_{nc} + F_{nu} - F_{nd} = (\gamma_s - \gamma_w m)z\cos^2\theta wl - \frac{1}{2}(K_p - K_a)z^2(\gamma_s - \gamma_w m^2)w\sin(\delta - \theta) \tag{14}$$

316 F_{nd} acts to decrease the normal force on the base of the central block when $\delta > \theta$, and to increase it

317 when $\delta < \theta$. The opposite is true of F_{nu}, however F_{nu} can also change sign in response to a negative active

318 force at the upslope margin. Given this definition of the normal force on its base, the basal resistance force

319 on the central block is then:

$$F_{rb} = C'_{rb} wl + F_{nt}\tan\phi' = (C'_{rb} + (\gamma_s - \gamma_w m)z\cos^2\theta\tan\phi')wl - \frac{1}{2}(K_p - K_a)z^2(\gamma_s - \gamma_w m^2)w\sin(\delta - \theta)\tan\phi' \tag{15}$$

320 3.5. Complete formulation

321 The Factor of Safety FS for the block can then be calculated as the ratio of driving to resisting forces

322 by combining each of these components from Equations 3, 7, 13, and 15:

$$FS = \frac{F_{rb} + 2F_{rc} + F_{rd} - F_{du}}{F_{dc}} \tag{16}$$

323 Substituting Equations 3, 7, 13 and 15 into 16 and rearranging, the general form of the equation is:

$$FS = \frac{\left(C'_{rb}+\cos^2\theta z(\gamma_s-\gamma_w m)\tan\varphi'\right)lw+\left(C'_{rl}+K_0\frac{1}{2}z(\gamma_s-\gamma_w m^2)\tan\varphi'\right)\cos\theta z2l+(K_p-K_a)\frac{1}{2}z^2(\gamma_s-\gamma_w m^2)w(\cos(\delta-\theta)-\sin(\delta-\theta)\tan\varphi')}{\sin\theta\cos\theta z\gamma_s lw} \quad (17)$$

324   In the upper-bound case we assume that $\delta = \phi'$ and Equation 17 becomes:

$$FS = \frac{\left(C'_{rb}+\cos^2\theta z(\gamma_s-\gamma_w m)\tan\varphi'\right)lw+\left(C'_{rl}+K_0\frac{1}{2}z(\gamma_s-\gamma_w m^2)\tan\varphi'\right)\cos\theta z2l+(K_p-K_a)\frac{1}{2}z^2(\gamma_s-\gamma_w m^2)w\left(\dfrac{\cos(2\varphi'-\theta)}{\cos\varphi'}\right)}{\sin\theta\cos\theta z\gamma_s lw} \quad (18)$$

325   In the lower-bound case we assume that $\delta = \theta$ and Equation 17 becomes:

$$FS = \frac{\left(C'_{rb}+\cos^2\theta z(\gamma_s-\gamma_w m)\tan\varphi'\right)lw+\left(C'_{rl}+K_0\frac{1}{2}z(\gamma_s-\gamma_w m^2)\tan\varphi'\right)\cos\theta z2l+\frac{1}{2}(K_p-K_a)z^2(\gamma_s-\gamma_w m^2)w}{\sin\theta\cos\theta z\gamma_s lw} \quad (19)$$

326   While these equations allow us to calculate the stability of a soil block, they do not include the

327 variability in soil properties, slope geometry and pore water pressure that occurs within an unstable

328 hillslope, which is an important control on slope stability in natural landscapes. In the following section we

329 apply the same equations within a grid-based framework, which allows us to represent spatial variability in

330 the model parameters.

3.6. Grid-based application

332   Following Hovland [1977] the normal and shear forces acting on the base of each column are derived

333 as components of their weight and FS is calculated from the ratio of total available resistance to the total

334 mobilized stress along the failure surface. As in Hovland [1977], we assume that there are no inter-column

335 shear forces within the group of columns that make up an unstable block. No progressive failure with strain

336 softening, pore water pressure dynamics, or other unequal stress-strain behavior is considered. The resistive

337 forces are applied to the outer boundary of the group of columns (i.e. the base and sides). Total resistance is

338 the sum of these basal and lateral components (Equations 7, 13 and 15). The total driving force is the vector

339 sum of the driving force vectors of each column within the potential landslide (Equation 3) and Figure 2).

340 Since the grid is not oriented slope-parallel most columns will have more than one force component

341 (upslope, downslope, cross-slope) acting on them. We decompose the lateral resistance on each column

342 margin into its components by assigning a fraction of the edge length to each resistance component. For

343 example, the upslope boundary of a grid cell that is oriented 30° from slope-parallel will be assigned 63%

344 upslope and 37% cross-slope resistance.

3.7.   Parameterization of cohesion

Cohesion acts on the base and lateral sides of a potential landslide and our model requires an assumption about the form of its variation with soil depth. Here we focus on colluvial slopes where the net soil cohesion is dominated by root strength [Schroeder and Alto, 1983; Schmidt, 1999]. Other forms of cohesion (e.g. due to cementation or suction) could easily be added given an expression for their variation with depth. Generally, root cohesion is not uniform with depth, as it is a function of root density, which typically declines exponentially with depth [e.g. Roering, 2008]. Following Dunne [1991] and Benda and Dunne [1997], we represent root cohesion as an exponential function of depth so that root cohesion on the basal failure plane C'_{rb} is defined as:

$$C'_{rb} = C'_{r0} e^{-zj} \tag{20}$$

where z is failure plane depth, C'_{r0} is a coefficient representing the maximum root cohesion value at the surface, and j is an e-folding length scale. Root cohesion can be integrated over the block depth z (in the vertical co-ordinate z_c) to obtain the average lateral root cohesion C'_{rl} per unit perimeter area:

$$C'_{rl} = \frac{1}{z} \int_0^z C'_{r0} e^{-z_c j} dz_c = \frac{C'_{r0}}{jz} \left(1 - e^{-zj}\right) \tag{21}$$

Equation 21 is applied to the cross-slope vertical boundaries and to the failure surfaces of the upslope and downslope wedges. When the downslope wedge failure surface is very curved this may result in a slight under-estimation of cohesion on this boundary. This is a necessary approximation because the iterative method developed by Soubra and Macuh [2002] requires profile-averaged cohesion.

4. Significance of model assumptions

Estimated earth pressure coefficients can vary widely depending on which formulation is used to calculate them. In section 4.1 we compare our earth pressure coefficients with those that have previously been used in other stability models discussed in section 2. In section 4.2 we assess the relative contribution of friction and cohesion to lateral resistance on an example slope and examine the sensitivity of the resistive terms to slope geometry and material properties.

4.1. Effect of different earth pressure coefficients

Figure 3a shows the earth pressure coefficients in a cohesionless soil as a function of slope angle using different methods of prediction. The simplest formulation estimates earth pressure by assuming that the ground surface is horizontal in the upslope (active) and downslope (passive) wedges and that there is no friction on the boundaries between the wedges and the central block. In this classic soil mechanics approach [Chen, 1981; Dietrich et al., 2008], earth pressure is only dependent on the friction angle. Using both upper- and lower-bound methods, the active K_{ah} and passive K_{ph} coefficients of earth pressure are the familiar:

$$K_{ah} = \tan^2 (45 - \frac{\phi'}{2}) \tag{22}$$

$$K_{ph} = \tan^2 (45 + \frac{\phi'}{2}) \tag{23}$$

and these pressures act perpendicular to the respective boundaries [Das, 2009].

Earth pressures predicted by the lower-bound (Rankine) and upper-bound (log-spiral and Coulomb) methods modified for sloping cohesionless soils illustrate the effects of slope angle (Figure 3a). The active pressure increases slightly at slopes between 38° and 40°, while the passive pressure declines sharply at steeper slopes until it equals the active pressure when the slope reaches the friction angle (here assumed to be 40°). The horizontal active earth pressure coefficient (K_{ah}) agrees well with the modified upper- and lower-bound coefficients, although it results in a slight underestimation of the active earth pressure when the slope is >38°. The passive coefficient assuming a horizontal ground surface (K_{ph}) falls between the upper- and lower-bound solutions for slopes gentler than 25° but results in a considerable overestimation of the passive earth pressure for slopes steeper than 25°, on which landslides are most likely.

On cohesionless slopes greater than the friction angle, earth pressure predictions become indeterminate for all the methods that account for sloping ground: the Rankine coefficients become complex because the square-root term in Equation 8 becomes negative; the Coulomb active coefficient goes to infinity because the failure surface that maximizes Equation 9 becomes parallel with the slope and the active wedge becomes infinitely long; and the log-spiral slip surface degenerates to a planar surface with radii approaching infinity, violating the optimization constraints [Soubra and Macuh, 2002].

390   In practice, cohesionless soil is rarely found on slopes steeper than the friction angle, as some cohesion

391   (provided by clay minerals, cementing agents, or more commonly vegetation roots) is usually necessary to

392   maintain soil mass stability on steep slopes [Das, 2009]. Figures 3b and c show the earth pressure

393   coefficients accounting for cohesion for two different scenarios: one where the cohesion is relatively low,

394   representing weak roots (Figure 3b) such as have been measured in grasslands [Buchanan and Savigny,

395   1990]; and another where the cohesion is larger, but still modest, representing a more dense root network or

396   stronger roots (Figure 3c) such as might be found in a forest [Schmidt *et al.*, 2001]. Figure 3 shows that even

397   a modest amount of additional cohesion considerably extends the range of slopes over which the earth

398   pressure coefficients can be predicted. Figure 3 also shows that when cohesion is included in the earth

399   pressure coefficient, the upper and lower bounds can cross at very high slopes suggesting that the treatment

400   of earth pressure is approximate for slopes steeper than the friction angle. However, the bounds do not

401   significantly diverge on high slopes, suggesting that the approximation is reasonable. In practice, shallow

402   landslides are not common on these extreme slopes where a soil mantle is unlikely to persist in the absence

403   of high cohesion.

4.2. Lateral strength contribution of friction

405   While lateral root cohesion has been included in a few stability models for natural slopes [Reneau and

406   Dietrich, 1987; Montgomery *et al.*, 2000, Gabet and Dunne, 2002; Casadei *et al.*, 2003a] lateral friction has

407   generally been ignored. Figure 4 compares the lateral resistance due to cohesion and friction on a cross-

408   slope margin and the net downslope resistance (i.e. resistance from the soil downslope of a block minus the

409   driving stress from the soil upslope). The example shown in Figure 4 is for a block with a failure plane depth

410   of 1 m, a friction angle of 40° and a saturation ratio of 0.5.

411   Friction on the cross-slope boundary provides ~2 kPa of resistance, independent of the block's

412   inclination (Figure 4). This suggests that cross-slope friction can be important in weakly rooted soils, as it is

413   nearly half of the resistance provided by roots (Figure 4). Cross-slope friction is highly sensitive to failure

414   plane depth (with a z^2 dependence) but insensitive to friction angle (Equation 7). This is because as the

415   friction angle increases, the earth pressure coefficient that controls the conversion from vertical to lateral

416 stress decreases as $1-\sin\phi'$, while shear strength varies as normal stress multiplied by $\tan\phi'$. The product of

417 these ($\tan\phi'$ $(1-\sin\phi')$) ranges from 0.26-0.30 for friction angles from 25°-55° with its maximum at 38°.

418   Net downslope resistance is considerably larger than cross-slope resistance (Figure 4). It is most

419 strongly dependent on cohesion but provides more strength than would be expected from cohesion alone,

420 increasing cohesion by 5 kPa in Figure 4 increases net resistance by between 8-15 kPa. This amplified

421 increase in resistance reflects the geometry of the upslope and downslope wedges. Since their failure surface

422 is always longer than the failure depth the additional strength is more than just the additional cohesion. Net

423 downslope resistance also has a strong (z^2) dependence on failure plane depth, a strong dependence on

424 slope, a weak dependence on saturation ratio, and negligible dependence on unit weight for both upper- and

425 lower-bound solutions with resistance increasing with depth and unit weight but decreasing with slope angle

426 and saturation ratio (Equation 12). Net resistance has a dependence on friction angle (not shown) that differs

427 between the two formulations, increasing with friction angle in the lower-bound case, and decreasing in the

428 upper-bound case. This reflects the influence of boundary friction (δ), which is assumed equal to soil

429 friction angle (ϕ') in the upper-bound case, in reducing net resistance. The influence of boundary friction is

430 absent from the lower-bound case (i.e. $\delta=0$) so that net resistance increases with soil friction, reflecting the

431 additional strength of the soil.

432 ## 5. A test of the model

433   To test the model, we applied it to the highly instrumented Coos Bay (CB-1) slope that failed as a

434 large debris flow in November 1996 [Anderson *et al.*, 1997; Montgomery *et al.*, 1997; Torres *et al.*, 1998;

435 Montgomery *et al.*, 2009]. We chose this site because, whereas there remains some uncertainty over the

436 geotechnical and hydrologic conditions appropriate for the site, the instrumentation at CB-1 provides one of

437 the most comprehensive data sets in existence for a natural shallow landslide. At CB-1 we tested the

438 model's ability to predict failure under the conditions measured during the 1996 storm, and whether the

439 predicted failure was of a similar size to that which was observed.

5.1. Test site description

The CB-1 site, which was clear-cut in 1987, is located along Mettman Ridge approximately 15 km north of Coos Bay in the Oregon Coast Range. The hydrological behavior of the CB-1 experimental site was studied in detail over a period of 10 years [Anderson *et al.*, 1997; Montgomery *et al.*, 1997; Torres *et al.*, 1998]. CB-1 is a 51 m long (860 m^2) unchanneled valley with an average slope of 43°. The instrumentation at CB-1 included a grid of piezometers and tensiometers with continuous total head measurements from 1990 to the time of failure (in 1996). Piezometer records show that subsurface storm flow in the shallow, fractured-rock zone exerts the most significant control on pore-pressure development in the CB-1 colluvium [Montgomery *et al.*, 1997]. We use the piezometric surface at the time of slope failure estimated by Montgomery *et al.* [2009] from piezometers recording at the time of failure, but without any adjustment of the original pore pressure data.

The soil is well-mixed, non-plastic gravelly sand derived from weathered turbidite sandstone [Schmidt *et al.*, 2001]. Low confining stress triaxial tests for samples from the site gave internal friction angles of 39.5° and 40° with effective soil cohesion of 0 to 1.8 kPa [Montgomery *et al.* 2009]. The soil bulk density (ρ_s) ranges from 1200 to 1600 kg m^{-3} [Schmidt *et al.*, 2001]. The soil thickness is well defined from soil borings [Schmidt, 1999]. Montgomery *et al.* [2009] measured basal and lateral root cohesions using the methods described by Schmidt *et al.* [2001]. They report a non-linear decline in root cohesion with depth resulting in a spatially-weighted average lateral root cohesion of 4.6 kPa and a basal cohesion of 0.1 kPa.

5.2. Method

On the basis of these observations, we back calculate the stability of the observed landslide under a set of 500 feasible site conditions sampled from distributions to account for uncertainty in observed conditions at the site. For each prediction, we provide a lower-bound on the stability estimate using the Rankine method and an upper-bound using the Coulomb (upslope) and log-spiral (downslope) methods. We assume a spatially uniform soil density and sample from a uniform distribution with range 1200-1600 kg m^{-3} (unit weight = 15.7 kN m^{-3}). We sample the friction angle from a normal distribution with mean 40° and standard deviation 2°; and the effective soil cohesion from a uniform distribution with the range 0-1.8 kPa. We use measured surface topography, soil depth and pore water pressure data interpolated to a 1 m grid (Figure 5a

467 and b). Topography and soil depth are very well constrained, we account for error in the pore water pressure

468 data by uniformly introducing normally distributed error with a standard deviation of 10%. To represent the

469 depth-varying lateral root cohesion we fit an exponential curve to the root cohesion with depth observations

470 of Montgomery *et al.* [2009] from the CB-1 site, with the additional constraint that the average lateral root

471 cohesion should be within ± 0.1 kPa of the spatially weighted mean lateral root cohesion observed at the

472 site. The best fit parameters within these constraints are C'_{r0} = 22 kPa and j = 4.96 m^{-1} (Equation 20); we

473 sample these parameters from normal distributions using these mean values and standard errors of: 0.5 kPa

474 and 0.73 m^{-1} respectively (ignoring covariance).

475 Montgomery *et al.* [2009] mapped the entire evacuated area at CB-1 and identified a smaller upper

476 section of the failure, which they suggest was the initiation area on the basis of their onsite observations.

477 Using the grid based formulation of MD-STAB, we test the stability of this initiation area by using its

478 geometry to define the group of potentially unstable columns in the stability model. To explore whether

479 smaller or larger shapes would result in different outcomes, we shrink and expand the original shape by a

480 constant distance around its perimeter and test their stability (Figure 5a).

481 **5.3. Results**

482 Figure 5c shows the factor of safety calculated from MD-STAB for the observed landslide geometry

483 and a series of smaller and larger conformal shapes. Instability is confined within a range of sizes for these

484 tested shapes. Shrinking the observed shape radially by 2 meters or expanding it by more than 5 meters

485 results in stability in more than 95% of cases (defined by the different parameter sets). This sets limits on the

486 possible size of the unstable area.

487 However, while most cases result in at least one stable shape many also predict at least one shape with

488 FS <1 (88% for lower-bound and 51% for upper-bound). This is not possible in reality since a landslide

489 would already have initiated as soon as driving force exceeded resistance. In the CB-1 case a model run that

490 predicts FS <1 for any shape is likely associated with an unrealistically weak parameter set and a run that

491 predicts FS>1 for all shapes with an unrealistically strong set. Failure, with FS=1, for the observed shape

492 and no other is associated with an intermediate parameter set for the upper-bound model and a high strength

493 parameter set for the lower-bound model (Figure 5c).

494   Of all the tested shapes, the observed landslide geometry is the least stable in 96% of cases. When size

495   decreases the area-perimeter ratio also decreases, reducing both driving and basal resisting forces relative to

496   the lateral resisting forces. When size increases under spatially variable conditions, the likelihood of

497   including areas of increased strength also increases. We suggest that the interaction of these two effects

498   defines an optimum, least stable, landslide geometry for a specific set of conditions. The CB-1 test shows

499   that without any calibration MD-STAB produces stability predictions for this slope that are consistent with

500   the observed landslide both in terms of its size and the conditions required for failure.

501   # 6. Discussion

502   ## 6.1. Critical depth and area

503   Smaller patches with low-strength conditions are more likely than larger ones in a natural

504   (heterogeneous) landscape, and thus in the absence of any other control the frequency of landslides should

505   continuously increase with decreasing size [Pellettier et al., 1997; Frattini and Crosta, 2013; Alvioli et al.,

506   2014]. Instead, many investigators have observed that there is a peak, or 'rollover', to the size frequency

507   distribution with fewer numbers of very small slides [e.g. Hovius et al., 1997; Stark and Hovius, 2001;

508   Malamud et al., 2004; Frattini and Crosta, 2013]. We suggest that the minimum area that can fail under a

509   given set of conditions (hereafter called the critical area) provides a mechanistic explanation of the

510   infrequency of small landslides while the right tail is controlled by the size distribution of low-strength areas

511   [Pelletier et al., 1997; Katz and Aharonov, 2006; Frattini and Crosta, 2013; Alvioli et al., 2014]. By setting

512   FS equal to 1.0, Equation 17 can be solved for the critical basal area A_c at failure:

$$A_c = \left(\frac{\left(2c'_{rl}z + K_0 z^2 (\gamma_s - \gamma_w m^2)\tan\varphi'\right)\cos\theta \left(\frac{l}{w}\right)^{\frac{1}{2}} + (K_p - K_a)\frac{1}{2}z^2(\gamma_s - \gamma_w m^2)(\cos(\delta-\theta)-\sin(\delta-\theta)\tan\varphi')\left(\frac{l}{w}\right)^{\frac{-1}{2}}}{\sin\theta\cos\theta z\gamma_s - c'_{rb} - \cos^2\theta z(\gamma_s - \gamma_w m)\tan\varphi'} \right)^2 \tag{24}$$

513   To explore how critical area changes with failure depth on a homogeneous slope, we examine a block

514   with the material properties measured at CB-1 (friction angle = 40°, soil unit weight = 15.7 kN m^{-3}, and

515   exponential cohesion profile with C_0=22 kPa and j=4.96) and a slope angle of 36°, the average slope for the

516   wider Coos Bay study area in which the landslide inventory shown in Figure 1 was collected [Montgomery

517   et al., 2000].

518   When soil strength is provided entirely by friction, A_c increases with depth from a minimum at the

519   surface (Figure 6), whereas when it is provided entirely by cohesion A_c decreases with depth from a

520   maximum at the surface (note log scale on vertical axis). This is because the stability of a soil block is

521   controlled by the relationship between its mass dependent driving force and the resistance on its perimeter

522   both of which vary with failure depth. Driving force increases linearly with depth but friction resistance

523   increases as the square of depth (z^2 terms on top half of Equation 24), while root cohesion decreases

524   exponentially with depth (Equations 20 and 21). When soil strength is provided by both friction and

525   cohesion ("Full" lines in Figure 6), the interplay between the two components results in a range of depths

526   with similar A_c, and a critical depth that minimizes A_c (indicated by filled circles in Figure 6). Although

527   there is a range of depths that are close to critical, failure planes that are both shallower and deeper than this

528   point are more stable and therefore require a larger A_c for failure (Figure 6). This is true for both upper- and

529   lower-bound solutions, which envelop the true value. These findings support those of Dietrich *et al.* [2008]

530   and Frattini and Crosta [2013] that suggest a least stable depth, and imply that this least stable depth

531   minimizes the critical area.

532   A critical depth in the range 0.5-3 m is consistent with observed shallow landslide depths (Figure 1c).

533   A parameter exploration (not shown) suggests that increasing cohesion (by increasing C_0 or by decreasing j)

534   or friction (by decreasing θ or increasing ϕ') results in a larger minimum critical area. However, increasing

535   cohesion increases the depth at which the minimum critical area occurs, while increasing friction decreases

536   it. Similar experiments (not shown) using uniform rather than depth-varying cohesion result in the same

537   behavior but with an increase in the depth at which the minimum critical area occurs. This is because, when

538   root cohesion is uniform, its contribution to basal resistance does not depend on depth, so its relative

539   contribution to total resistance is very large at shallow depths and decreases rapidly with depth. Decreasing

540   cohesion with depth simply enhances this effect. Figure 6 also shows that the difference between the upper-

541   and lower-bound earth pressure solutions is large when cohesion is included and negligible when only

542   friction is considered.

543   The critical area and the corresponding failure depth for this parameter set are in the range observed

544   for shallow landslides (Figure 1a and c), and closely correspond to the modal landslide depth and area for

545   landslides from the Coos Bay site on which the parameters have been based (Figure 6; Montgomery [1991];

546   Larsen et al. [2010]). However, where soils are shallower than the critical depth, landslides will be very

547   likely to fail at the soil-bedrock interface rather than within the harder bedrock. This is generally the case at

548   Coos Bay, where most landslides failed at the soil bedrock interface [Montgomery et al., 2000], which may

549   explain the portion of observed Coos Bay failures with depths less than our prediction.

550   As noted above, the predicted critical depth and area can be close to zero in the case of a saturated

551   cohesionless soil (Figure 6). This motivates the question: are there any constraints on critical depth and area

552   for cohesionless soils? To address this we examine the behavior of a cohesionless block of soil 5 m long, 5

553   m wide, and 2 m deep, with a friction angle of 40° and a soil unit weight of 15.7 kN m^{-3}. The slope angle is

554   reduced from the average slope of the Coos Bay site to 30° to reflect the characteristics of cohesionless

555   slopes. We test the stability of this block using Equation 17 for slope-parallel failure planes at depths from

556   0.02 m to 10 m in increments of 0.01 m, beginning with an unsaturated block and increasing the water table

557   height until failure occurs within the block.

558   Under dry conditions, the block is stable for all failure plane depths and FS increases linearly with

559   depth (red curve in Figure 7a). This is because both the driving force and basal resistance increase linearly

560   with depth, and lateral resistance increases as the square of depth (Equation 17). With a water table of 0.2 m

561   below the ground surface or lower, the block remains stable at any depth (i.e. FS>1) but there is a minimum

562   FS within the profile (blue curves in Figure 7). When the failure plane is above the water table FS is the

563   same as in the unsaturated case. Once the failure plane is below the water table the saturated fraction of the

564   soil column above the failure plane increases with failure plane depth causing FS to decrease. FS reaches a

565   minimum at 1.2 m then begins to increase (blue curves in Figure 7a) because the lateral resistance increases

566   at a higher rate compared to the reduction of shear resistance resulting from the increase of the saturated soil

567   fraction (Equation 24). If the water table continues to rise, the block will fail at ~0.8 m depth once the water

568   table reaches 0.09 m depth (black curves in Figure 7a). As the water table approaches the surface, FS

569   continues to decrease (cyan curve in Figure 7a).

570   Figure 7b shows that as the water table rises both the critical area and critical depth decrease. As the

571   water table approaches the ground surface, the critical depth approaches zero and the critical area declines

572   rapidly. When the water table reaches the ground surface the saturated fraction of the soil column no longer

573   varies with depth, and the minimum FS is at the surface (green curve in Figure 7a) due to the more rapid

574   increase of resisting force relative to driving force with depth (Equation 24). This explains why the critical

575   failure plane depth and critical landslide size are both zero for cohesionless saturated soils (green curve in

576   Figure 7b). Note that there is a critical area when $Z_w = 0.2$ ($A_c = 75$ m^2), indicating that failure is possible at

577   this water table depth but requires a much larger size than the 5 by 5 m block used in Figure 7a. The dry

578   case is stable at any area since the slope is shallower than the friction angle and thus it has no critical area

579   and does not appear in the bottom panel of Figure 7.

580   For a specific set of conditions, in a cohesive or cohesionless soil the water table height determines

581   both the critical size and critical failure depth. Instability can occur when the area having that water table

582   height expands to the critical size, or when a local increase of the water table sufficiently reduces the critical

583   size. This suggests that the dynamics of the water table are an important control on landslide size and that

584   topography exerts a strong control on landslide size not only through on local slope but also through its

585   influence on soil depth and water table height. These results also suggest that while cohesion leads to a

586   minimum landslide size [Reneau and Dietrich, 1987, Dietrich et al., 2008; Frattini and Crosta, 2013], slide

587   size is limited even in cohesionless landscapes. This provides a physical basis for a rollover in the landslide

588   size distribution, albeit at a considerably smaller size than commonly reported [e.g. Hovius 1997; Stark and

589   Hovius, 2001; Malamud et al. 2004; Stark and Guzzetti 2009].

590   **6.2.   Critical shape**

591   While it is commonly observed that landslide length exceeds width [Gabet and Dunne, 2002; Rickli, *et*

592   *al.*, 2008; Marchesini *et al.*, 2008], this behavior has not been fully explained. In a second set of experiments

593   using the saturated cohesive scenario (θ=36°, ϕ'=40°, γ_s=15.7 kN m^{-3}, C_0=22 kPa, j=4.96), we explore the

594   impact of shape (in terms of the length-width ratio) on FS and critical area of a potential landslide. We

595   calculate FS and critical area of blocks of depth 0.5, 1, 2 and 5 m, varying the length-width ratio from 0.01

596   to 100 to find the ratio that minimizes FS and critical area (Figure 8). Here we show only results using the

597   lower-bound earth pressure formulation (i.e. Rankine's method), which is conservative in terms of its

598   predicted FS, critical area and depth because it predicts shallower failures with a smaller minimum area.

599   Results (not shown) using the upper-bound earth pressure formulation generally exhibit similar behavior,

600   but differ slightly in their absolute values, due to the increased resistance on the upslope and downslope

601   margins.

602   The least stable shape is that which minimizes resisting force relative to driving force. When lateral

603   strength is provided by cohesion alone (dashed lines in Figure 8) the least stable shape is equi-dimensional

604   (i.e. l/w=1 minimizes FS and A_c) independent of block depth, because this minimizes perimeter length for a

605   given area. Once a friction component is introduced, resistance on the upslope and downslope margins

606   dominates (Figure 4), and scales with the cross-sectional area of these margins. On natural slopes failure

607   depth is limited by soil depth (typically to a maximum of a few meters). Width is thus the main control on

608   the cross-sectional area of the upslope and downslope margins, leading to wider shapes having a higher FS

609   for a given area (Figure 8a) or a larger critical area (Figure 8b). FS and critical area increase again when l/w

610   ratio is greater than 3 as the perimeter to area ratio is then large enough to overcome the effect of the

611   strength difference between the margins.

612   The least stable shapes (marked with solid dots in Figure 8) are consistently longer than they are wide.

613   The least stable l/w ratio increases with increasing block depth from 1.5 to 5, due to the increased strength

614   on the downslope margin. This is because, as depth increases, a greater fraction of the resistance is provided

615   by friction, and the strength on the downslope boundary becomes more important. A parameter exploration

616   (not shown) suggests that length exceeds width for all parameter combinations except when the slope

617   exceeds the friction angle.

618   These results imply that for similar size low-strength patches, the patch that is oriented with its long

619   axis downslope should be less stable. This is consistent both with the general observation that shallow

620   landslide scars are longer than they are wide (Figure 1b) and with the l/w ratios of landslides observed in the

621   Coos Bay catchment, which was used to parameterize the model (Figure 8b; Montgomery [1991]).

622   However, it is unlikely that the strength difference between the downslope and cross-slope margins is the

623   sole reason for this pattern. The shape of an unstable patch is controlled by the spatial pattern of the driving

624   parameters (particularly pore water pressure and soil depth), which is not random, but rather is strongly

625   controlled by topography and often oriented with greater values in the downslope direction.

6.3.   Depth–area scaling

627   Finally, we explore the relationship between critical area and the depth that minimizes that area. We

628   perform a set of numerical experiments where soil unit weight and friction angle are held constant at the

629   values measured at CB-1. We test a range of slopes with different combinations of slope angle (θ = 20°, 30°

630   and 40°), root cohesion (C_0= 0, 1 22 and 52 kPa; j = 4.96 m^{-1}) and water table depth (0-10 m in 0.02 m

631   increments). These conditions represent typical ranges for landscapes in which shallow landslides occur. For

632   each combination, failure planes are tested (in 0.02 m increments) from the surface to the base of the soil

633   column to find the minimum critical area and record its corresponding depth. For simplicity, only the lower-

634   bound solutions (i.e. from Rankine's method) are shown in Figure 9. The upper-bound solutions (using

635   Coulomb and log-spiral methods) result in slightly larger critical areas.

636   The curves in Figure 9 show critical area and depth for slopes with the same material properties but

637   varying saturation, for different cohesion scenarios. They are compared to a global compilation of

638   observations from Larsen et al. [2010]. In the cohesionless case there is an approximately square-root

639   relationship between critical area and depth (Figure 9a). All but one of the observations have scar areas that

640   exceed those defined by the 40° curve. When cohesion is introduced, critical area and depth both decrease

641   with increasing saturation following a similar square-root relationship to a lower limit at fully saturated

642   conditions (filled circles in Figure 9b-d). However, on natural slopes soil depth is often less than a few

643   meters and many landslides have their failure plane at the base of the soil [e.g. Montgomery et al., 2000].

644   When landslide depth is limited by soil depth (as suggested by Larsen et al. [2010]), the failure surface is

645   forced to the base of the soil column and critical area increases as soil depth decreases (dashed colored lines

646   in Figure 9b-d). This is because the resistance due to root cohesion becomes increasingly dominant relative

647   to the driving force. The dashed colored lines in Figure 9 represent the minimum critical area occurring

648   under fully-saturated conditions. Reducing saturation results in an increase of critical area at a given depth

649   (not shown).

650   Varying the slope angle has a strong impact on the coefficient but a weak impact on the exponent of

651   the depth-area relationship, suggesting similar scaling behavior independent of the material properties. The

652   three cohesion scenarios shown in Figure 9b-d encompass conditions from weak grassland to strong natural

653   forest root networks. When cohesion is low (Figure 9b), the depth-area curve provides a lower bound to the

654   observations. Increasing cohesion results in curves that encompass progressively fewer observations (Figure

655   9c-d). Our results show that increasing cohesion increases both the minimum landslide depth and critical

656   area, suggesting that in landscapes with stronger cohesion landslides should be both larger and deeper

657   consistent with observations [e.g. Selby, 1976; Gabet and Dunne, 2002].

658   The roughly square-root dependence of depth on area is consistent with the observations; the best fit

659   for observed soil landslides yields an exponent of 0.4 [Larsen et al., 2010]. In cohesionless soils, the

660   predicted exponent is always 0.5 and Equation 16 can be rearranged to solve for depth in terms of critical

661   area:

$$z = kA_c^{\frac{1}{2}} \tag{24}$$

662   where

$$k = \frac{\sin\theta\cos\theta\gamma_s - \cos^2\theta\left(\gamma_s - \gamma_w m\right)\tan\phi'}{K_0\left(\gamma_s - \gamma_w m^2\right)\tan\phi'\cos\theta\left(\dfrac{l}{w}\right)^{\frac{1}{2}} + \left(K_p - K_a\right)\dfrac{1}{2}\left(\gamma_s - \gamma_w m^2\right)\left(\cos(\delta-\theta) - \sin(\delta-\theta)\tan\phi'\right)\left(\dfrac{l}{w}\right)^{\frac{-1}{2}}} \tag{25}$$

663   When cohesion is introduced the lateral resistance becomes a more complex function of depth and

664   thus the exact relationship becomes dependent on the specific conditions, how cohesion is parameterized,

665   and the relative importance of friction and cohesion.

666   The modelled depth-area curves represent the critical failure plane depth and the minimum landslide

667   area for a given set of conditions. Our findings differ from those of Klar *et al.* [2011] in that we suggest that

668   depth only imposes a lower bound on size, whereas they suggested that area defines depth. As a result our

669   model only explicitly explains the trend in observed minimum landslide area with depth, which is well

670   captured by the $\theta = 40°$ curve in Figure 9b. However, since smaller low-strength patches are likely to be

671   more common in a natural (heterogeneous) landscape [Pelletier, 1997; Frattini and Crosta, 2013], we might

672   expect landslide areas to cluster near their lower size limit, explaining the similar trend in maximum

673   landslide area for a given depth with the majority of the data plotting between the modelled 20° and 30°

674 curves (Figure 9). We suggest that our model is an alternative explanation of the observed landslide depth-

675 area scaling to that of Klar *et al.* [2011], both based on limit equilibrium slope stability models. Since Klar

676 et al. find the depth area scaling from experiments in which length is constrained their approach might

677 suggest that landslide area is set first (e.g. by slope length or the area of a low strength patch) and that

678 landslide depth is then dependent on this area. Since we find the critical (or minimum) landslide area for a

679 given landslide depth our approach might suggest that depth is set first (e.g. by pore pressure or soil depth)

680 and that landslide area is then dependent on depth. Both situations are conceivable on natural slopes and it is

681 interesting that both approaches result in approximately square root relationships between landslide depth

682 and area.

683 **6.4. Model assumptions and requirements**

684 MD-STAB is a shallow landslide slope stability model and as such is limited in its application to

685 failures within or at the base of the soil. In common with most other shallow landslide models, our model

686 assumes that failure occurs under drained conditions. This is appropriate for the colluvial soils found on

687 many natural slopes but not for clay-rich materials.

688 Our model also assumes hydrostatic conditions in the calculation of active and passive pressures on

689 the upslope and downslope margins of the central block. In reality slope parallel seepage will alter these

690 pressures but we currently lack methods that account for them. A reduction in net downslope resistance due

691 to seepage forces would slightly reduce critical area, increase optimum depth, and make the least stable

692 shape slightly rounder. However, this does not alter our general findings that: 1) there is a critical area and

693 minimum depth for both cohesive and cohesionless soils; 2) blocks that are longer than they are wide are

694 least stable; and 3) critical area scales as the square of optimum depth under most conditions found in

695 natural landscapes.

696 Jaky's [1944] empirical formula, which assumes cohesionless soil, may overestimate the cross-slope

697 earth pressure coefficient. However, resistance due to at-rest earth pressure on the cross slope boundary is

698 small relative to other components (Figure 4), so small changes to the value of K_0 will have little impact on

699 the net resistance. To assess the potential impact of this assumption we tested the extreme case of neglecting

700 the cross-slope earth pressure term (i.e. $K_0=0$) and found that our results show very little sensitivity to the

701 value of this coefficient. Moreover, changes in K_0 do not alter the linear dependence of at-rest earth pressure

702 on depth, which drives our findings on optimum depth and depth-area scaling.

703 In our model the landslide is assumed to have a parallelepipedal shape, with vertical sides. The

704 assumption that cross-slope margins are vertical rather than inclined or curved will minimize their surface

705 area and resulting resistance [Stark and Eid, 1998]. This is consistent with field observations, which suggest

706 that the head scarps of shallow landslides are generally near-vertical and that their cross-slope margins are

707 also steep. Failure geometry at the downslope boundary is poorly constrained by observations, because of

708 subsequent erosion following failure. Nevertheless, where observation has been possible, a low angle failure

709 surface generally connects the ground surface with the basal failure plane [Milledge, 2008], consistent with

710 the wedge representation used here. The assumption that the failure plane is parallel to the ground surface is

711 reasonable for shallow translational landslides where the radius of curvature of the failure surface is

712 typically very low, and enables us to limit the search space for critical failure depth to one dimension.

713 In MD-STAB the potential failure mass is treated a rigid block although in reality a failure may occur

714 progressively if small-scale cracks coalesce into a continuous failure plane [Petley, *et al.*, 2005] or locally

715 high strain induces liquefaction [Iverson *et al.*, 2000]. At present representing such progressive failure is

716 generally limited to computationally-intensive continuum methods, although Lehmann and Or [2012] have

717 developed an innovative approach to represent this progressive failure implicitly. We have applied our

718 boundary force equations within a limit-equilibrium framework to examine their implications for landslide

719 size and shape. However, we note that our equations could easily be applied within a framework similar to

720 that of Lehman and Or [2012], which would account for the forces acting on the margins due to the self-

721 weight of the soil, and would result in a more appropriate method for natural slopes.

722 The parameters required to run MD-STAB are the same as those required to evaluate the infinite slope

723 equation: surface slope and friction angle, soil cohesion and unit weight, failure plane depth, and water table

724 height. Several of these parameters are either derived from or strongly influenced by topography; for

725 example, local slope, soil depth and pore water pressure could be modelled in a similar way to Dietrich *et al.*

726 [1995, 2008]. Other parameters are likely to vary in space, but the magnitude and correlation length of their

727 variability are unknown in most landscapes so that they are generally assumed spatially uniform as we have

728 done here. Cohesion due to roots is likely to vary with depth below the surface. There is reasonable

729   observational support for an exponential relationship between root cohesion and depth in many landscapes

730   [Hales *et al.*, 2009] enabling root cohesion to be simply represented with the addition of only one parameter.

731   However, MD-STAB is not bound to this particular representation, requiring only a root strength field.

732   Similarly, we have chosen a very simple representation of pore water pressure (assuming steady slope-

733   parallel flow), but more complex alternatives that provide a pore pressure field could be utilized. The only

734   additional data requirement for MD-STAB is the identification of cells that are within the shape whose

735   stability is to be tested. However, this is a key barrier to the model's application to a discretized landscape.

736   While stability can be calculated analytically for each potential landslide, testing all possible combinations

737   of cells would be exponentially complex; the number of tests goes as $2^{(nrows*ncols)}$ or 10,000 combinations for

738   a 10 by 10 cell grid. In a forthcoming paper this model is coupled with a novel search algorithm to predict

739   landslides across a landscape [D. Bellugi, D.G. Milledge, W.E. Dietrich, J. McKean, J.T. Perron, E.

740   Sudderth and B. Kazian, A spectral clustering search algorithm for predicting shallow landslide size and

741   location, submitted to JGR-Earth Surface 2013; D. Bellugi, D.G. Milledge, W.E. Dietrich, J. McKean, and

742   J.T. Perron, Predicting shallow landslide size and location across a natural landscape: Application of a

743   spectral clustering search algorithm, submitted to JGR-Earth Surface 2013].

744   # 7. Conclusion

745   In this paper we derive MD-STAB, a new multi-dimensional shallow slope stability model that

746   predicts the observed shallow landslide depth-area scaling in both cohesive and cohesionless soils arises

747   from depth-varying friction on the margins of a potential landslide. MD-STAB accounts for the forces

748   acting on all boundaries of a potential landslide and is statically determinate. It represents lateral root

749   cohesion and earth pressure on inclined slopes, making it suitable for natural landscapes. This model is

750   easily applied to spatially gridded data, requires only a modest parameterization (i.e. the same as the infinite

751   slope), and is therefore suitable for landscape-scale application.

752   MD-STAB successfully predicts the failure of a well-documented shallow landslide in which

753   measured parameters, including pore pressure and root strength, are used. The model also predicts that

754   larger or smaller shapes conformal to that observed are indeed more stable. For smaller shapes stability is

755 due to the increased influence of resistance on the margins, whereas for larger shapes stability is due to the

756 inclusion of areas of increased strength.

757   We explore the influence of lateral friction and cohesion on slope stability and landslide scale (depth

758 and area) using an inclined block of soil with fixed strength parameters but varying pore pressure and soil

759 depth. Lateral friction on the boundaries of a potential landslide increases considerably the magnitude of

760 lateral reinforcement. Friction and cohesion interact to create a critical depth at which shallower and deeper

761 potential failure planes are more stable. This critical depth develops even in cohesionless soils when they are

762 less than fully saturated. As a result, landslides should have a minimum area for failure in both cohesive and

763 cohesionless soils. Friction and cohesion also impose a least stable shape that is longer than it is wide, even

764 in homogeneous hillslope conditions. Minimum scar area is predicted to increase as approximately the

765 square of failure plane depth, consistent with and bounding observed landslide depth-area data.

766   These findings suggest that a peak, or rollover, in observed landslide size-frequency distributions

767 should be expected, and that the observed depth-area scaling is related to the depth-varying lateral frictional

768 resistance. We hypothesize that the right tail of observed landslide size-frequency distributions is controlled

769 by the heterogeneity of local conditions. Exploring this hypothesis will require applying this model to real

770 landscapes to determine size and location of landslides under a variety of conditions.

771 # **Appendix 1**

772   Below are the equations for the log-spiral earth pressure representation for sloping soils that include

773 both friction and cohesion strength following Soubra and Macuh [2002].

774

$$k_{p\gamma} = -k_{a\gamma} = \frac{2}{\left(\dfrac{z}{r^0}\right)^2} \frac{f1 - f2 - f3}{f4} \tag{A1}$$

$$k_{pc} = k_{ac} = \frac{1}{\dfrac{z}{r^0}} \frac{f7 - f5}{f4} \tag{A2}$$

$$f1 = \pm \left[\frac{e^{3(\alpha_1 - \alpha_0)\tan\varphi}\left(3\tan\varphi\sin\alpha_1 \pm \cos\alpha_1\right) \pm 3\tan\varphi\sin\alpha_0 + \cos\alpha_0}{3\left(9\tan^2\varphi + 1\right)} \right] \tag{A3}$$

$$f2 = \pm \frac{1}{6}\frac{L}{r_0}\left(2\sin\alpha_0 + \frac{L}{r_0}\cos\theta\right)\cos(\alpha_1 - \theta)e^{\mp(\alpha_1 = \alpha_0)\tan\varphi} \tag{A4}$$

$$f3 = \pm\frac{1}{6}\frac{z}{r_0}2\sin^2\alpha_0 \tag{A5}$$

$$f4 = \begin{cases} \cos\delta\left(\cos\alpha_0 - \frac{1}{3}\frac{z}{r_0}\right)\pm\sin\delta\sin\alpha_0 & for\,K_\gamma \\ \cos\delta\left(\cos\alpha_0 - \frac{1}{2}\frac{z}{r_0}\right)\pm\sin\delta\sin\alpha_0 & for\,K_c \end{cases} \tag{A6}$$

$$f5 = \pm\frac{z}{r_0}\frac{\tan\delta}{\tan\varphi}\sin(-\alpha_0) \tag{A7}$$

$$f7 = \mp\frac{1}{2\tan\varphi}\left(e^{\mp2(\alpha_1-\alpha_0)\tan\varphi} - 1\right) \tag{A8}$$

$$\frac{L}{r_0} = \frac{e^{3(\alpha_1-\alpha_0)\tan\varphi}\sin\alpha_1 - \sin\alpha_0}{\cos\theta} \tag{A9}$$

$$\frac{z}{r_0} = \frac{-e^{\mp(\alpha_1-\alpha_0)\tan\varphi}\cos(\alpha_1-\theta) + \cos(\alpha_0-\theta)}{\cos\theta} \tag{A10}$$

775

776

Acknowledgements

Notation

Variable	Units	Description
A_c	m^2	critical basal area of the central block required for failure
C'_{r0}	Pa	coefficient representing the maximum root cohesion value at the surface

C'_{rb}	Pa	root cohesion on the basal failure surface
C'_{rl}	Pa	depth averaged lateral root cohesion
F_{dc}	N	central block driving force
F_{du}	N	slope-parallel component of the active force
F_{nc}	N	normal force central block weight force acting on the failure surface
F_{nd}	N	slope normal component of the passive force
F_{nt}	N	total normal force acting on the basal failure surface of the central block
F_{nu}	N	slope normal component of the active force (negative for a net resisting force) on the upslope margin of the central block
F_p	N	passive force
F_{rc}	N	resisting force on each cross-slope side of the slide block
F_{rd}	N	slope-parallel component of the passive force
FS	-	factor of safety
F_w	N	central block weight force
g	m s^{-2}	gravitational acceleration
h	m	water table height above failure surface
j	m^{-1}	e-folding length scale for root cohesion with depth in the soil profile
K_0	-	coefficient of at-rest earth pressure
K_a	-	active earth pressure coefficient
K_{ah}	-	horizontal active earth pressure coefficient
K_p	-	passive earth pressure coefficient
K_{ph}	-	horizontal passive earth pressure coefficient
K_{pc}	-	cohesion component of Soubra and Macuh's [2002] passive earth pressure coefficient
$K_{p\gamma}$	-	friction component of Soubra and Macuh's [2002] passive earth pressure coefficient
l	m	true downslope length of the slide block
m	-	saturation ratio
s_c	Pa	resisting stress on the cross-slope sides of the slide block
w	m	cross-slope width of the slide block
x_c	m	cross-slope planimetric coordinate
y_c	m	down-slope planimetric coordinate
z_c	m	vertical coordinate
z	m	failure surface depth below the ground surface
z_w	m	water table depth below the ground surface
α_0, α_1	°	geometry parameters for the logarithmic-spiral failure surface
β	°	inclination from horizontal of failure plane from base of central block to ground surface upslope
δ	°	boundary friction angle
γ_s	N m^{-3}	unit weight of the soil
γ_w	N m^{-3}	unit weight of water
ϕ'	°	soil friction angle
ρ_s	kg m^{-3}	bulk density of soil
σ'_x	Pa	at-rest lateral earth pressure
σ'_z	Pa	vertical effective pressure

σ_a	Pa	active stress on the upslope margin of the central block
σ_p	Pa	passive stress on the downslope margin of the central block
σ_z	Pa	total vertical geostatic stress
θ	°	slope inclination
τ	Pa	driving stress

References

785 Alvioli, M., F. Guzzetti, and M. Rossi (2014), Scaling properties of rainfall induced landslides predicted by
786 a physically based model, *Geomorphology*, 213, 38-47.
787
788 Anderson, S. P., W. E. Dietrich, D. R. Montgomery, R. Torres, M. E. Conrad, and K. Loague (1997),
789 Subsurface flow paths in a steep, unchanneled catchment, *Water Resources Research*, 33(12), 2637-2653.

790 Baum, R. L., J. W. Godt, and W. Z. Savage (2010), Estimating the timing and location of shallow rainfall-
791 induced landslides using a model for transient, unsaturated infiltration, *Journal of Geophysical Research:*
792 *Earth Surface (2003–2012)*, 115(F3).

793 Baum, R. L., W. Z. Savage, and J. W. Godt (2008), TRIGRS - a fortran program for transient rainfall
794 infiltration and grid-based regional slope stability analysis, version 2.0, *Open File Rep.*, 81 pp, U.S.
795 Geological Survey.

796 Benda, L., and T. Dunne (1997), Stochastic forcing of sediment supply to channel networks from
797 landsliding and debris flow, *Water Resources Research*, 33(12), 2849-2863.

798 Buchanan, P., K. W. Savigny, and J. Devries (1990), A method for modeling water tables at debris
799 avalanche headscarps, *J. Hydrol.*, 113(1-4), 61-88.

800 Burroughs, E. R. J. (1985), Landslide hazard rating for portions of the Oregan Coast range paper presented
801 at Symposium on effects of forest land use on erosion and slope stability, University of Hawaii, Honolulu,
802 HI.

803 Caquot, A., and J. Kerisel (1948), *Tables de poussee et de butee*, Gauthier-Villars, Paris.

804 Casadei, M., W. E. Dietrich, and N. L. Miller (2003a), Controls on shallow landslide size, in *Debris-Flow*
805 *Hazards Mitigation: Mechanics, Prediction, and Assessment*, edited by D. Rickenmann and C. Chen, pp. 91-
806 101.

807 Casadei, M., W. E. Dietrich, and N. L. Miller (2003b), Testing a model for predicting the timing and
808 location of shallow landslide initiation in soil-mantled landscapes, *Earth Surface Processes and*
809 *Landforms*, 28(9), 925-950.

810 Chen, W. F. (1975), *Limit analysis and soil plasticity*. Elsevier Science, Amsterdam.

811 Chen, R. H. (1981), Three-dimensional slope stability analysis, *JHRP Rep.*, 81-17 pp, Purdue University.

812 Chugh, A. K. (2003), On the boundary conditions in slope stability analysis, *International Journal for*
813 *Numerical and Analytical Methods in Geomechanics*, 27(11), 905-926.

814 Chugh, A. K., and J. D. Smart (1987), Discussion of "Active Earth Pressure Behind Retaining Walls" by
815 Sangchul Bang (March, 1985, Vol. 111, No. 3), *Journal of Geotechnical Engineering*, 113(8), 930-932.

Coulomb, C. A. (1776), Essai sur une application des regles des maximis et minimis a quelques problemes de statique relatifs a l'architecture, *Memoires de l'Achademie Royale pres Divers Savants*, *7*.

Craig, R. F. (2004). *Craig's soil mechanics*. CRC Press.

Das, B. (2009), *Principles of geotechnical engineering*, seventh ed., Cengage Learning, Stamford, Connecticut.

Dietrich, W. E., J. McKean, D. Bellugi, and J. T. Perron (2008), The prediction of shallow landslide location and size using a multidimensional landslide analysis in a digital terrain model., in *Proceedings of the Fourth International Conference on Debris-Flow Hazards Mitigation*, edited.

Dietrich, W. E., R. Reiss, M. L. Hsu, and D. R. Montgomery (1995), A Process-Based Model for Colluvial Soil Depth and Shallow Landsliding Using Digital Elevation Data, *Hydrological Processes*, *9*(3-4), 383-400.

Duncan, J. M. (1996), State of the art: Limit equilibrium and finite-element analysis of slopes, *Journal of Geotechnical Engineering-ASCE*, *122*(7), 577-596.

Duncan, J. M., and R. L. Mokwa (2001), Passive earth pressures: theories and tests, *Journal of Geotechnical and Geoenvironmental Engineering*, *127*(3), 248-257.

Dunne, T. (1991), Stochastic aspects of the relations between climate, hydrology and landform evolution, *Transactions of the Japanese Geomorphological Union*, *12*, 1-12.

Epanechnikov, V. A. (1969), Non-parametric estimation of a multivariate probability density, *Theory of Probability & Its Applications*, *14*(1), 153-158.

Fellenius, W. (1936), Calculation of the stability of earth dams, paper presented at Second Congress on Large Dams, Washington D.C.

Frattini, P., and G. B. Crosta (2013), The role of material properties and landscape morphology on landslide size distributions, *Earth and Planetary Science Letters*, *361*, 310-319.

Gabet, E. J., and T. Dunne (2002), Landslides on coastal sage-scrub and grassland hillslopes in a severe El Nino winter: The effects of vegetation conversion on sediment delivery, *Geological Society of America Bulletin*, *114*(8), 983-990.

Gnanapragasam, N. (2000), Active earth pressure in cohesive soils with an inclined ground surface, *Canadian Geotechnical Journal*, *37*(1), 171-177.

Griffiths, D. V., and R. M. Marquez (2007), Three-dimensional slope stability analysis by elasto-plastic finite elements, *Geotechnique*, *57*(6), 537-546, doi:10.1680/geot.2007.57.6.537.

Guzzetti, F., F. Ardizzone, M. Cardinali, M. Rossi, and D. Valigi (2009), Landslide volumes and landslide mobilization rates in Umbria, central Italy, *Earth and Planetary Science Letters*, *279*(3), 222-229.

Haefeli, R. (1948), The stability of slopes acted upon by parallel seepage, paper presented at International Conference on Soil Mechanics and Foundation Engineering.

Hales, T., C. Ford, T. Hwang, J. Vose, and L. Band (2009), Topographic and ecologic controls on root reinforcement, *Journal of Geophysical Research: Earth Surface (2003–2012)*, *114*(F3).

Hovius, N., C. P. Stark, and P. A. Allen (1997), Sediment flux from a mountain belt derived by landslide mapping, *Geology*, *25*(3), 231-234.

854 Hovland, H. J. (1977), 3-Dimensional Slope Stability Analysis Method, *Journal of the Geotechnical*
855 *Engineering Division-Asce*, *103*(9), 971-986.

856 Hungr, O., S. McDougall, M. Wise, and M. Cullen (2008), Magnitude–frequency relationships of debris
857 flows and debris avalanches in relation to slope relief, *Geomorphology*, *96*(3), 355-365.

858 Iverson, R., M. Reid, N. Iverson, R. LaHusen, M. Logan, J. Mann, and D. Brien (2000), Acute sensitivity of
859 landslide rates to initial soil porosity, *Science*, *290*(5491), 513-516.

860 Iverson, R. M. (2000), Landslide triggering by rain infiltration, *Water Resources Research*, *36*(7), 14.

861 Jaky, J. (1944), The coefficient of earth pressure at rest, *Journal of the Union of Hungarian Engineers and*
862 *Architects*, 355-358.

863 Katz, O., and E. Aharonov (2006), Landslides in vibrating sand box: What controls types of slope failure
864 and frequency magnitude relations? *Earth and Planetary Science Letters*, 247(3), 280-294. DOI:
865 10.1016/j.epsl.2006.05.009.

866 Klar, A., E. Aharonov, B. Kalderon-Asael, and O. Katz (2011), Analytical and observational relations
867 between landslide volume and surface area, *Journal of Geophysical Research: Earth Surface (2003–*
868 *2012)*, *116*(F2).

869 Lam, L. and D.G. Fredlund (1993), A general limit equilibrium model for 3-D slope stability analysis,
870 *Canadian Geotechnical Journal*, 30: 905-919.

871 Lanni, C., M. Borga, R. Rigon, and P. Tarolli (2012), Modelling shallow landslide susceptibility by means
872 of a subsurface flow path connectivity index and estimates of soil depth spatial distribution, *Hydrology &*
873 *Earth System Sciences*, *16*(11).

874 Larsen, I. J., D. R. Montgomery, and O. Korup (2010), Landslide erosion controlled by hillslope
875 material, *Nature Geosci*, *3*(4), 247-251.

876 Lasdon, L. S., A. D. Waren, A. Jain, and M. Ratner (1978), Design and testing of a generalized reduced
877 gradient code for nonlinear programming, *ACM Transactions on Mathematical Software (TOMS)*, *4*(1), 34-
878 50.

879 Lehmann, P., and D. Or (2012), Hydromechanical triggering of landslides: From progressive local failures
880 to mass release, *Water Resources Research*, *48*(3).

881 Malamud, B. D., D. L. Turcotte, F. Guzzetti, and P. Reichenbach (2004), Landslide inventories and their
882 statistical properties, *Earth Surface Processes and Landforms*, *29*(6), 687-711, doi:10.1002/esq.1064.

883 Marchesini, I., C. Cencetti, and P. De Rosa (2009), A preliminary method for the evaluation of the
884 landslides volume at a regional scale, *Geoinformatica*, *13*(3), 277-289.

885 Mazindrani, Z., and M. Ganjali (1997), Lateral earth pressure problem of cohesive backfill with inclined
886 surface, *Journal of geotechnical and geoenvironmental engineering*, *123*(2), 110-112.

887 Milledge, D. G. (2008), Modelling shallow landslides: the importance of hydrological controls and lateral
888 reinforcement, Ph.D. thesis, 466 pp, Durham University, Durham.

889 Montgomery, D. R. (1991), Channel initiation and landscape evolution, Ph.D. thesis, University of
890 California, Berkeley, California.

891 Montgomery, D. R., and W. E. Dietrich (1994), A Physically-Based Model for the Topographic Control on
892 Shallow Landsliding, *Water Resources Research*, *30*(4), 1153-1171.

893 Montgomery, D. R., W. E. Dietrich, R. Torres, S. P. Anderson, J. T. Heffner, and K. Loague (1997),
894 Hydrologic response of a steep, unchanneled valley to natural and applied rainfall, *Water Resources*
895 *Research*, *33*(1), 91-109.

896 Montgomery, D. R., K. M. Schmidt, W. E. Dietrich, and J. McKean (2009), Instrumental record of debris
897 flow initiation during natural rainfall: Implications for modeling slope stability, *Journal of Geophysical*
898 *Research: Earth Surface (2003–2012)*, *114*(F1).

899 Montgomery, D. R., K. M. Schmidt, H. M. Greenberg, and W. E. Dietrich (2000), Forest clearing and
900 regional landsliding, *Geology*, *28*(4), 311-314.

901 Morgan, B. A., G. Wieczorek, R. Campbell, and P. Gori (1997), *Debris-flow hazards in areas affected by*
902 *the June 27, 1995 storm in Madison County, Virginia*, US Geological Survey.

903 Morgenstern, N.R. and V.E. Price (1965) The analysis of the stability of general slip surfaces,
904 *Geotechnique*, 15(1), 79–93.

905 Mullins, C., and K. Panayiotopoulos (1984), The strength of unsaturated mixtures of sand and kaolin and the
906 concept of effective stress, *Journal of Soil Science*, *35*(3), 459-468.

907 Paudel, P. P., K. Moriwaki, K. Morita, T. Kubota, and H. Omura (2003), An assessment of shallow
908 landslides mechanism induced by rainfall in Hakoishi Area, *Kyushu Journal of Forest Research*, *56*, 122-
909 128.

910 Pelletier, J. D., B. D. Malamud, T. Blodgett, and D. L. Turcotte (1997), Scale-invariance of soil moisture
911 variability and its implications for the frequency-size distribution of landslides, *Engineering Geology*, *48*(3-
912 4), 255-268.

913 Petley, D. N., T. Higuchi, D. J. Petley, M. H. Bulmer, and J. Carey (2005), Development of progressive
914 landslide failure in cohesive materials, *Geology*, *33*(3), 201-204.

915 Piegari, E., V. Cataudella, R. Di Maio, L. Milano, and M. Nicodemi (2006), A cellular automaton for the
916 factor of safety field in landslides modeling, *Geophysical research letters*, 33(1), L01403, DOI:
917 10.1029/2005GL024759.

918 Qiu, C., T. Esaki, M. Xie, Y. Mitani, and C. Wang (2007), Spatio-temporal estimation of shallow landslide
919 hazard triggered by rainfall using a three-dimensional model, *Environmental Geology*, *52*(8), 1569-1579.

920 Rankine, W. (1857), On the stability of loose earth, *Philosophical Transactions of the Royal Society of*
921 *London*, *147*.

922 Reneau, S. L., and W. E. Dietrich (1987), Size and location of colluvial landslides in a steep forested
923 landscape, paper presented at Proceedings of the International Symposium on Erosion and Sedimentation in
924 the Pacific Rim.

925 Rice, R. M., E. Crobett, and R. Bailey (1969), Soil slips related to vegetation, topography, and soil in
926 southern California, *Water Resources Research*, *5*(3), 647-659.

927 Rickli, C., S. Kamm, and H. Bucher (2008), Ereignisanalyse Hochwasser 2005, Teilprojekt Flachgründige
928 Rutschungen. , *Projektbericht zuhanden des Bundesamtes für Umwelt, BAFU Rep.*, p. 112 S. pp.

Roering, J. J. (2008), How well can hillslope evolution models "explain" topography? Simulating soil transport and production with high-resolution topographic data, *Geological Society of America Bulletin*, *120*(9-10), 1248-1262.

Schmidt, K. M. (1999), Root strength, colluvial soil depth, and colluvial transport on landslide-prone hillslopes, Ph.D. thesis, University of Washington, Seattle, Washington.

Schmidt, K. M., J. J. Roering, J. D. Stock, W. E. Dietrich, D. R. Montgomery, and T. Schaub (2001), The variability of root cohesion as an influence on shallow landslide susceptibility in the Oregon Coast Range, *Canadian Geotechnical Journal*, *38*(5), 995-1024.

Selby, M. (1976), Slope erosion due to extreme rainfall: a case study from New Zealand, *Geografiska Annaler. Series A. Physical Geography*, 131-138.

Skempton, A. W., and F. A. DeLory (1957), Stability of natural slopes in London clay, paper presented at 4th International Conference on Soil Mechanics and Foundation Engineering.

Soubra, A.-H. (2000), Static and seismic passive earth pressure coefficients on rigid retaining structures, *Canadian Geotechnical Journal*, *37*(2), 463-478.

Soubra, A.-H., and B. Macuh (2002), Active and passive earth pressure coefficients by a kinematical approach, *Proceedings of the ICE-Geotechnical Engineering*, *155*(2), 119-131.

Spencer, E. (1967), A method of analysis of the stability of embankments assuming parallel interslice forces, *Geotechnique*, *17*(1), 11-26.

Spiker, E. C., and P. Gori (2003), *National landslide hazards mitigation strategy, a framework for loss reduction*, US Geological Survey, Reston, Virginia.

Stark, C. P., and F. Guzzetti (2009), Landslide rupture and the probability distribution of mobilized debris volumes, *J. Geophys. Res.-Earth Surf.*, *114*, 16, doi:F00a0210.1029/2008jf001008.

Stark, C. P., and N. Hovius (2001), The characterization of landslide size distributions, *Geophysical Research Letters*, *28*(6), 1091-1094.

Stark, T. D., and H. T. Eid (1998), Performance of three-dimensional slope stability methods in practice, *Journal of Geotechnical and Geoenvironmental Engineering*, *124*(11), 1049-1060.

Tarolli, P., and D. G. Tarboton (2006), A new method for determination of most likely landslide initiation points and the evaluation of digital terrain model scale in terrain stability mapping, *Hydrology and Earth System Sciences*, *10*(5), 663-677.

Taylor, D. W. (1948), *Fundamentals of Soil Mechanics*, Wiley, New York.

Terzaghi, K. (1967), *Theoretical soil mechanics*, 510 pp., John Wiley & Sons, New York.

Terzaghi, K., and R. B. Peck (1967), *Soil mechanics in engineering practice, 2nd edition*, John Wiley & Sons, New York.

Torres, R., W. E. Dietrich, D. R. Montgomery, S. P. Anderson, and K. Loague (1998), Unsaturated zone processes and the hydrologic response of a steep, unchanneled catchment, *Water Resources Research*, *34*(8), 1865-1879.

965   Warburton, J., D. G. Milledge, and R. M. Johnson (2008), Assessment of shallow landslide activity
966   following the January 2005 storm, Northern Cumbria, *Proceedings of the Cumberland Geological*
967   *Society*, 7, 263-283.

968   Zhu, D.-Y., and Q. Qian (2000), Determination of passive earth pressure coefficients by the method of
969   triangular slices, *Canadian geotechnical journal*, *37*(2), 485-491.

Figures

Figure 1: Observed landslide properties from six published inventories showing empirical PDFs of: (a) landslide scar area; (b) scar depth; (c) scar length (L) to width (W) ratio and (d) a scatter plot showing the power relationship between scar depth and area. The inventories are from: (1) the Appalachian mountains [Morgan et al., 1997]; (2) Hakoishi, Japan [Paudel et al., 2003]; (3) San Gabriel Mountains, California [Rice et al., 1969]; (4) Santa Barbara County, California [Gabet and Dunne, 2002]; (5) Cumbria, England [Warburton et al., 2008]; and (6) Oregon Coast Range [Montgomery, 1991; Larsen et al., 2010]. Grey diamonds in (d) are the scar dimensions for soil landslides from a global compilation by Larsen et al. [2010]. PDFs are generated using kernel density functions after Epanechnikov [1969], with optimized half widths given in brackets in each legend.
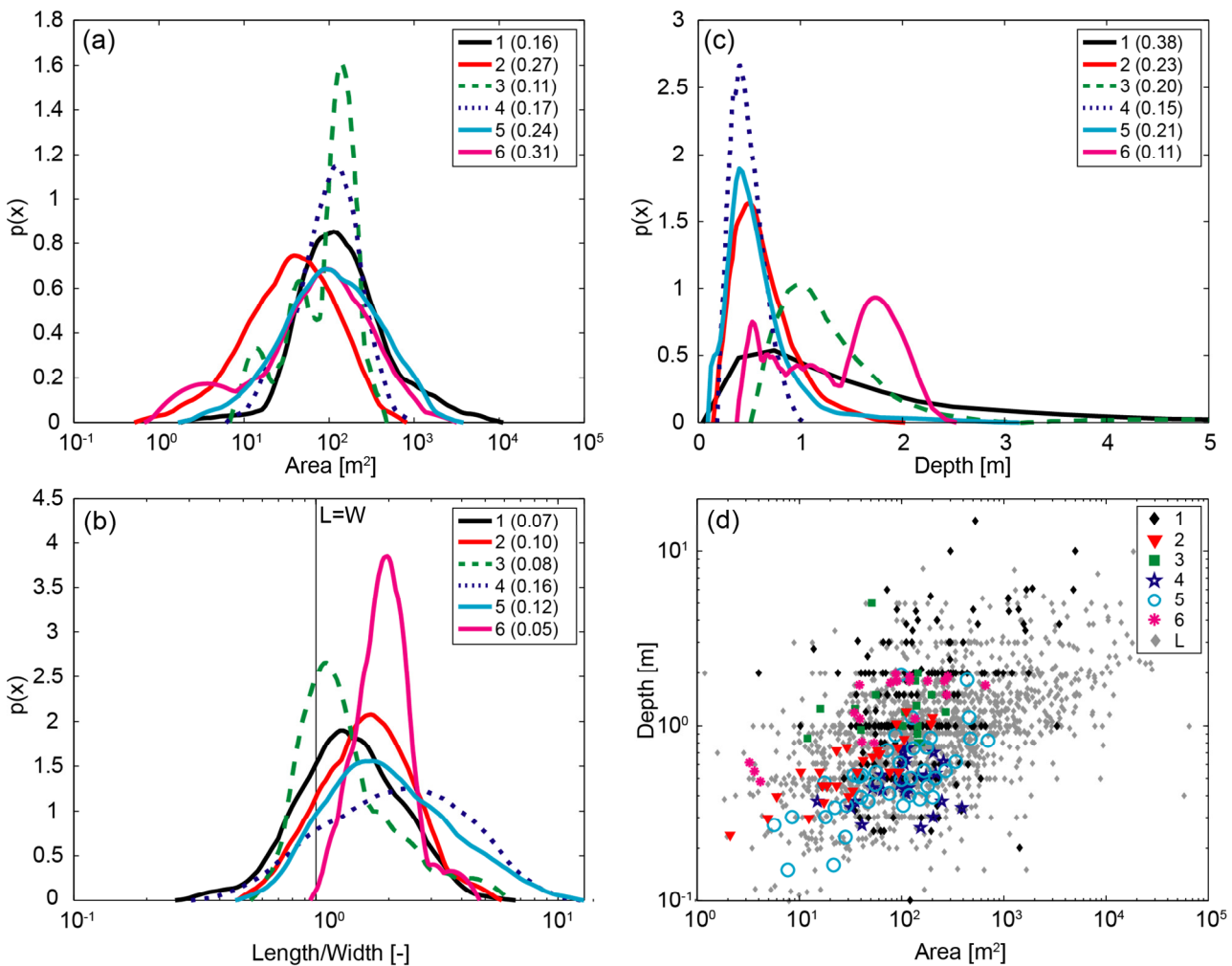
Figure 2: Schematic showing forces and lengths for the three-dimensional slope stability problem in: (a) 3D, (b) cross-section, (c) profile and (d) plan. MD-STAB computes the stability of a potential landslide by calculating the forces on each of the planes shown here. The red arrows in (a), (c), and (d) show the forces acting on each margin of the block. The red arrows in (b) show the stress distribution on the cross-slope sides of the block. Red force polygons P1-6 in (c) and (d) illustrate the magnitude and orientation of forces acting on the block and their combination (i.e. vector sum) to give resultant forces: (P1) normal and driving forces on the central block; (P2) active force on the upslope margin; (P3) passive force on the downslope margin; (P4) normal and resisting forces on the base central block; (P5) and (P6) normal and resisting forces on the cross-slope sides.
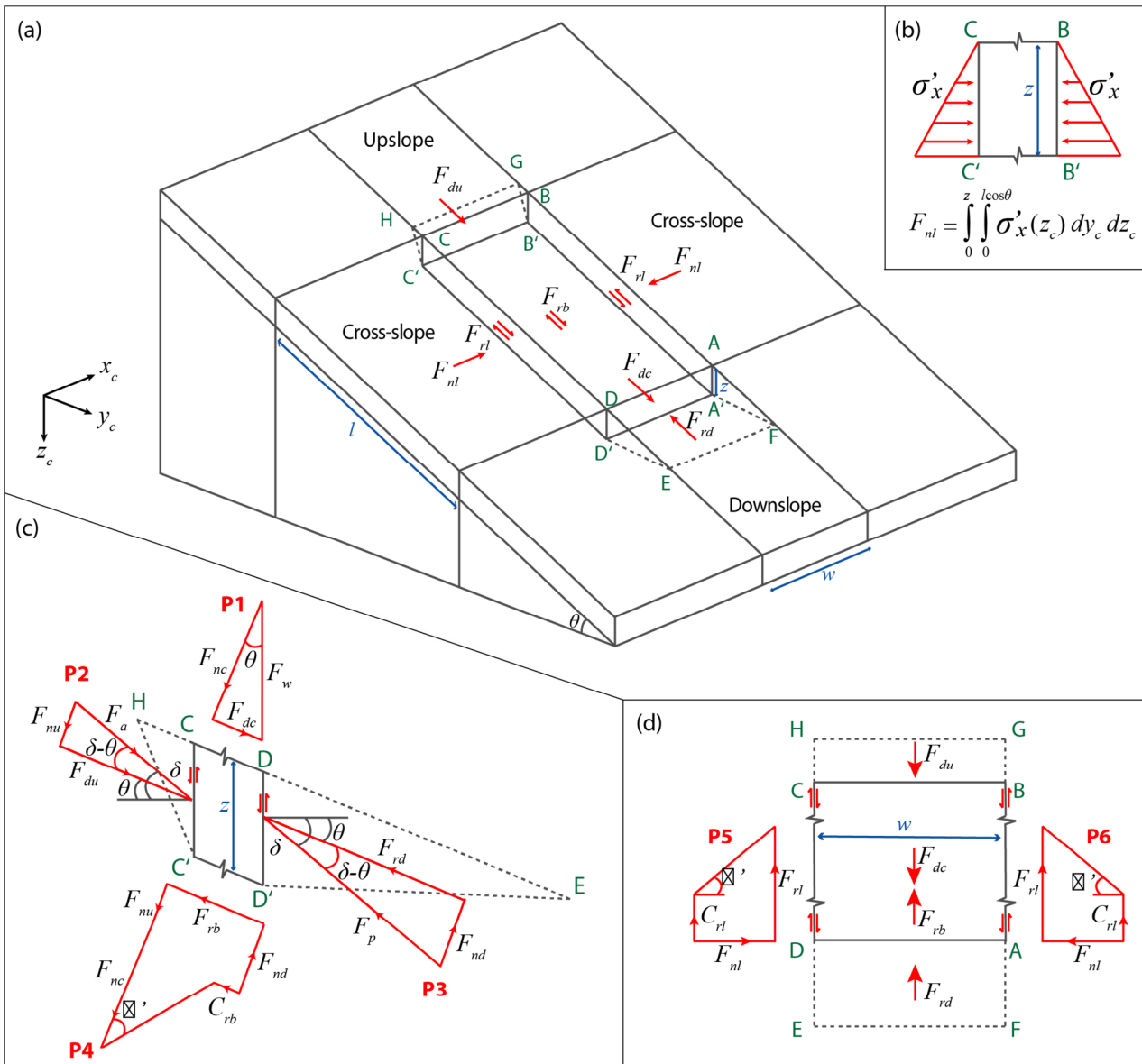
994   *Figure 3: Earth pressure coefficients calculated using different methods. Parameter values used*

995   *are: z=1; θ=0-60°; m=1; φ'=40°; γ$_s$=15.7 kN m^{-3}; and (a) C'$_{rl}$=0 kPa, (b) 1kPa, and (c) 5kPa. Shaded*

996   *areas are defined by the upper- and lower-bound solutions. All lower-bound solutions are derived using*

997   *the Rankine method. Upper-bound solutions for the active case at the head of a landslide are by the*

998   *Coulomb method and for the passive case at the slide toe the solutions are by the log-spiral method. The*

999   *horizontal coefficient results in an overestimate of passive resistance on steep slopes. The coefficients that*

000   *account for sloping soils become indeterminate on cohesionless slopes greater than the friction angle.*

001   *This problem is reduced by representing cohesion in the earth pressure coefficient (panels b and c). Note*

002   *that in this case the upper-bound coefficient can fall below the lower-bound coefficient at very high*

003   *slopes suggesting that the treatment of earth pressure is approximate for slopes steeper than the friction*

004   *angle.*

005

006
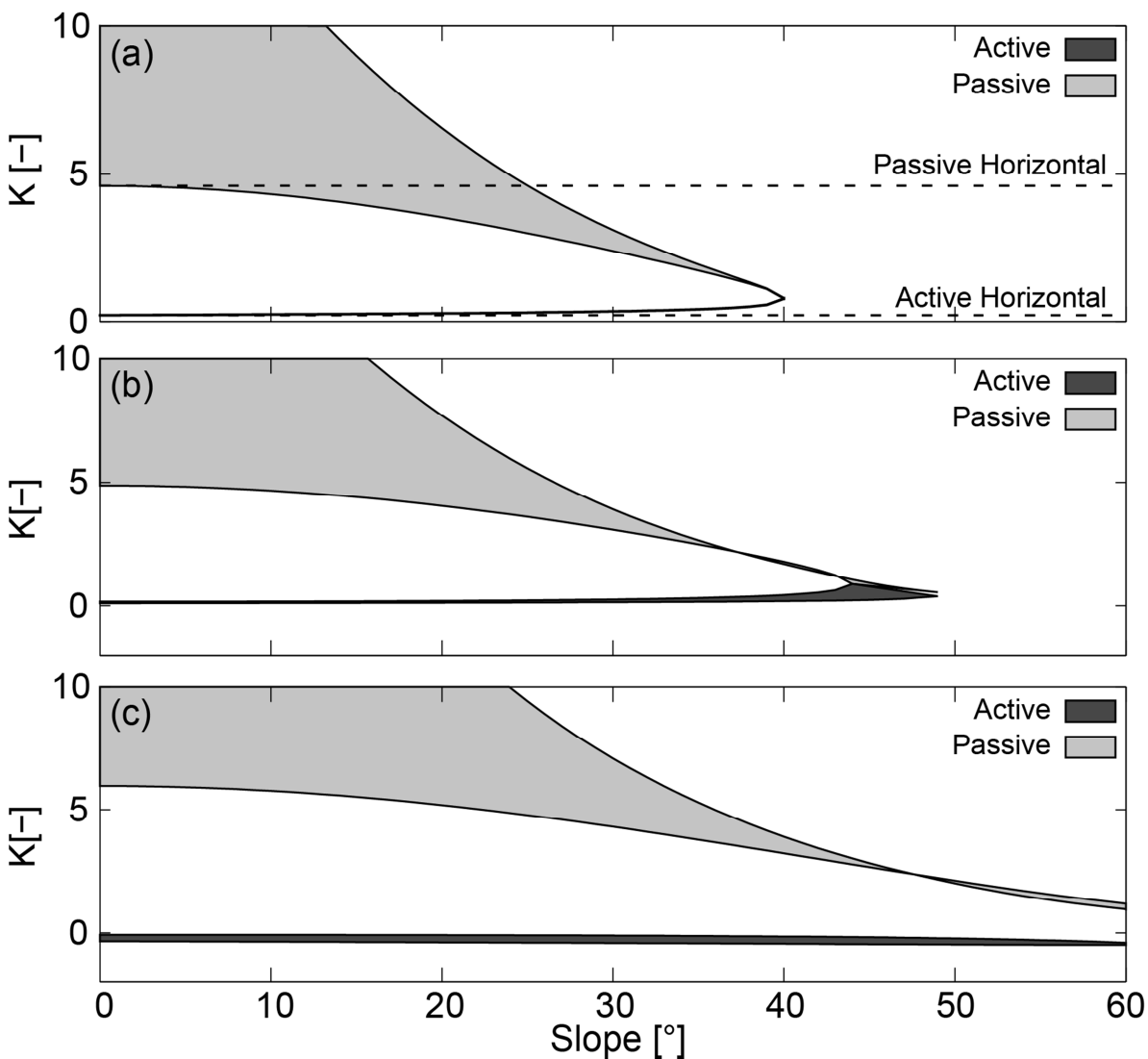
Figure 4: Lateral and net downslope resistances from different strength components at different slope angles for a block of soil with γ_s=15.7 kN m^{-3}, ϕ'=40°, z=1 m, and m=0.5, for a weak roots case (C'$_{rl}$=5 kPa) and a stronger roots case (C'$_{rl}$=10 kPa). Shaded areas are defined by the upper- and lower-bound earth pressure solutions. Cohesion and cross-slope friction are invariant with slope. The net resistance on the downslope margin (i.e. downslope resistance - upslope drive) is always more than twice as large as the root cohesion, and becomes more important on shallower slopes.
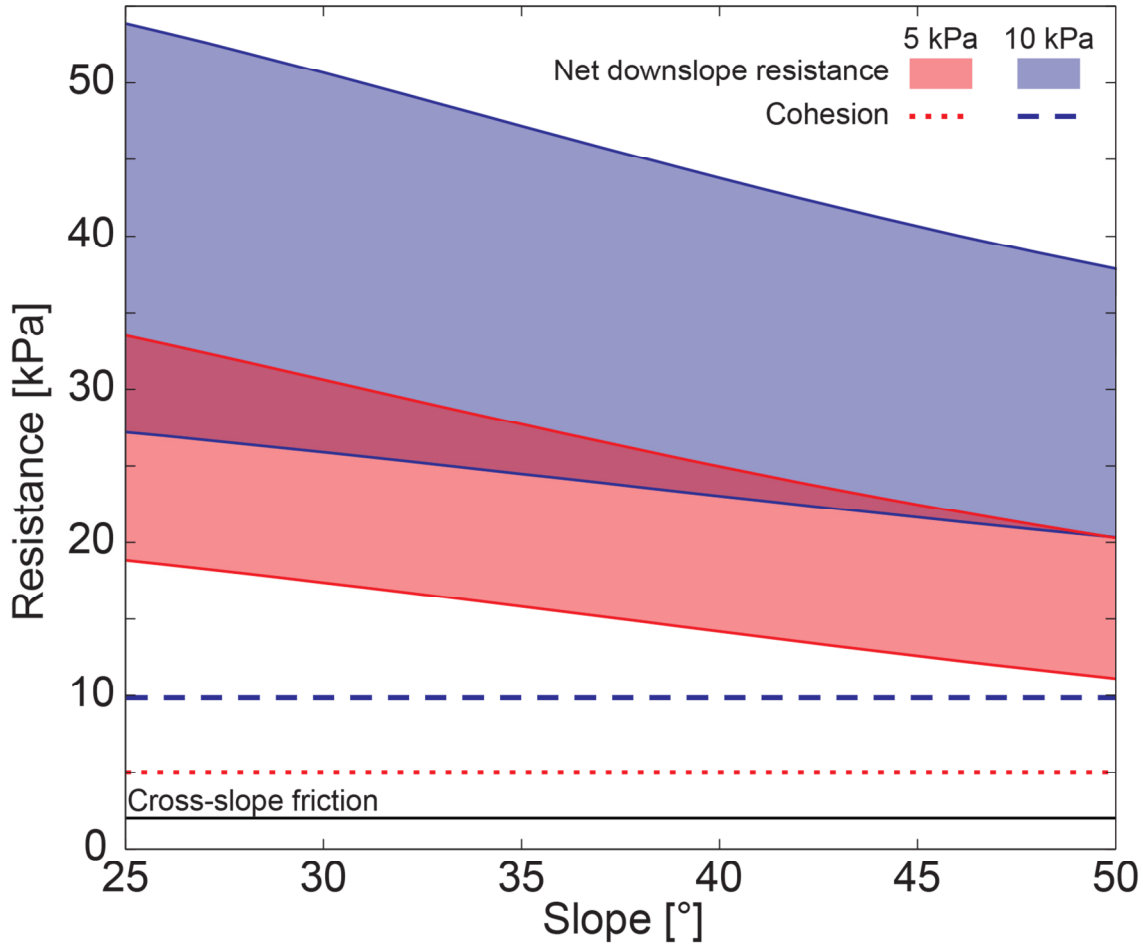
Figure 5: Model application to the CB-1 hillslope (Oregon, USA). (a) Map of the site showing the observed landslide scar (red), and the larger and smaller conformal shapes (blue) tested for stability. White contours show elevation (m), greyscale contours show soil depth (m). (b) Map showing elevation contours in black and piezometric surface contours in blue (m), soil unit weight (γ_s=15.7 kN m^{-3}), friction angle (~40°) and root cohesion (~4 kPa) are also well constrained at the site. (c) The predicted factor of safety for the observed landslide (size growth = 0) and smaller and larger shapes generated by expanding and contracting the observed landslide geometry by a radial distance indicated on the x-axis. Upper (blue) and lower (red) bounds are obtained using upper- and lower-bound earth pressure solutions. Pale lines show each of the 500 model runs described in Section 5.2. thick dark lines show the mean FS from these runs +/- 1 standard deviation. Panels: a) and b) are modified from Montgomery et al. [2009]. The model predicts failure for the observed scar geometry and finds that larger or smaller conformal shapes are more stable.
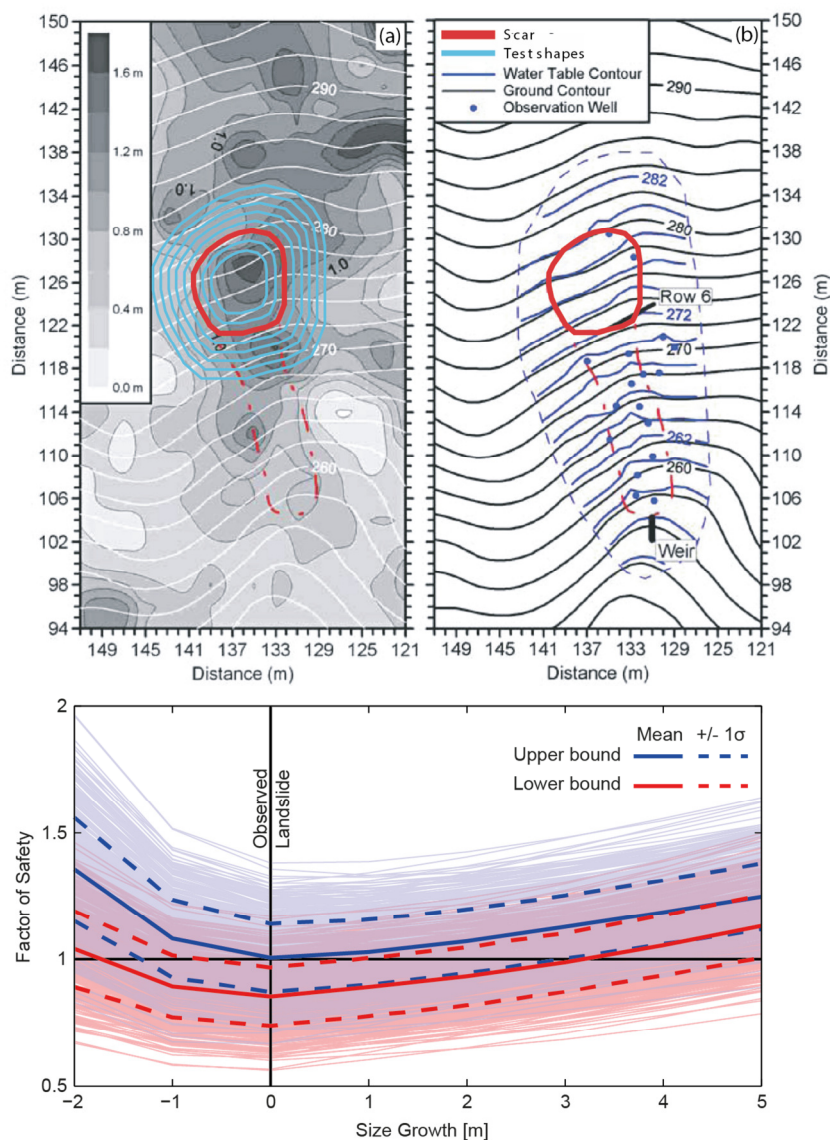
Figure 6 critical area with depth for an equi-dimensional homogeneous block of soil at a slope of 36°, friction angle of 40°, γ_s=15.7 kN m^{-3} with a water table at the ground surface (i.e. fully saturated soil), assuming a l/w ratio of 1 (representative of the CB-1 scar). Note logarithmic y-axis. Red dots show the depths at which the critical area is minimized (A_c=23 m^2 at z=1.9 m in the lower-bound case and A_c=42 m^2 at z=2.18 m in the upper-bound case). Shaded areas are defined by the upper- and lower-bound earth pressure solutions in the friction-only case these nearly coincide and the cohesion-only case does not have upper and lower bounds. The grey PDFs on the x and right axes show depths and area distributions respectively for 19 landslides in the Coos Bay catchment [Montgomery, 1991; Larsen et al., 2010].
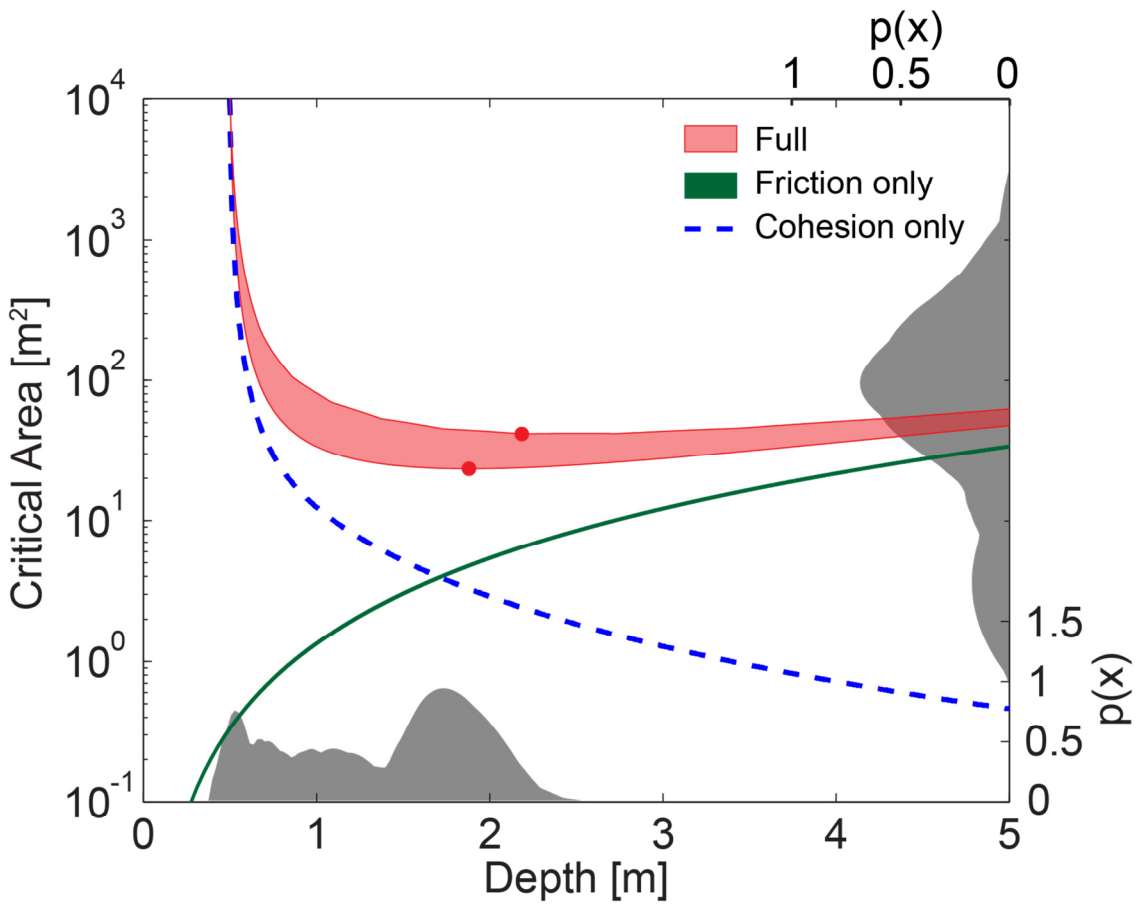
038   *Figure 7: the factor of safety (a) and critical area (b) with depth for a block of soil where θ=30°,*

039   *ϕ'=40°, γ_s=15.7 kN m^{-3}, for a range of water table depths (Z_w). In both panels there are two lines for each*

040   *water table depth, representing upper- and lower-bound solutions. The symbols above each plot indicate*

041   *water table locations within the profile. Panel (a) shows the factor of safety for a 5 x 5 m block while*

042   *panel (b) shows the critical block area A_c, which can vary. The dry case is stable at any area since*

043   *$\tan\phi'$>$\tan\theta$ thus it has no critical area and does not appear in panel (b); the case of z_w=0.2 is stable for*

044   *the 5 x 5 m block but appears in panel (b) because it becomes unstable for critical areas > 75 m^2. Both*

045   *factor of safety and critical area are minimized within the profile for partially saturated conditions.*
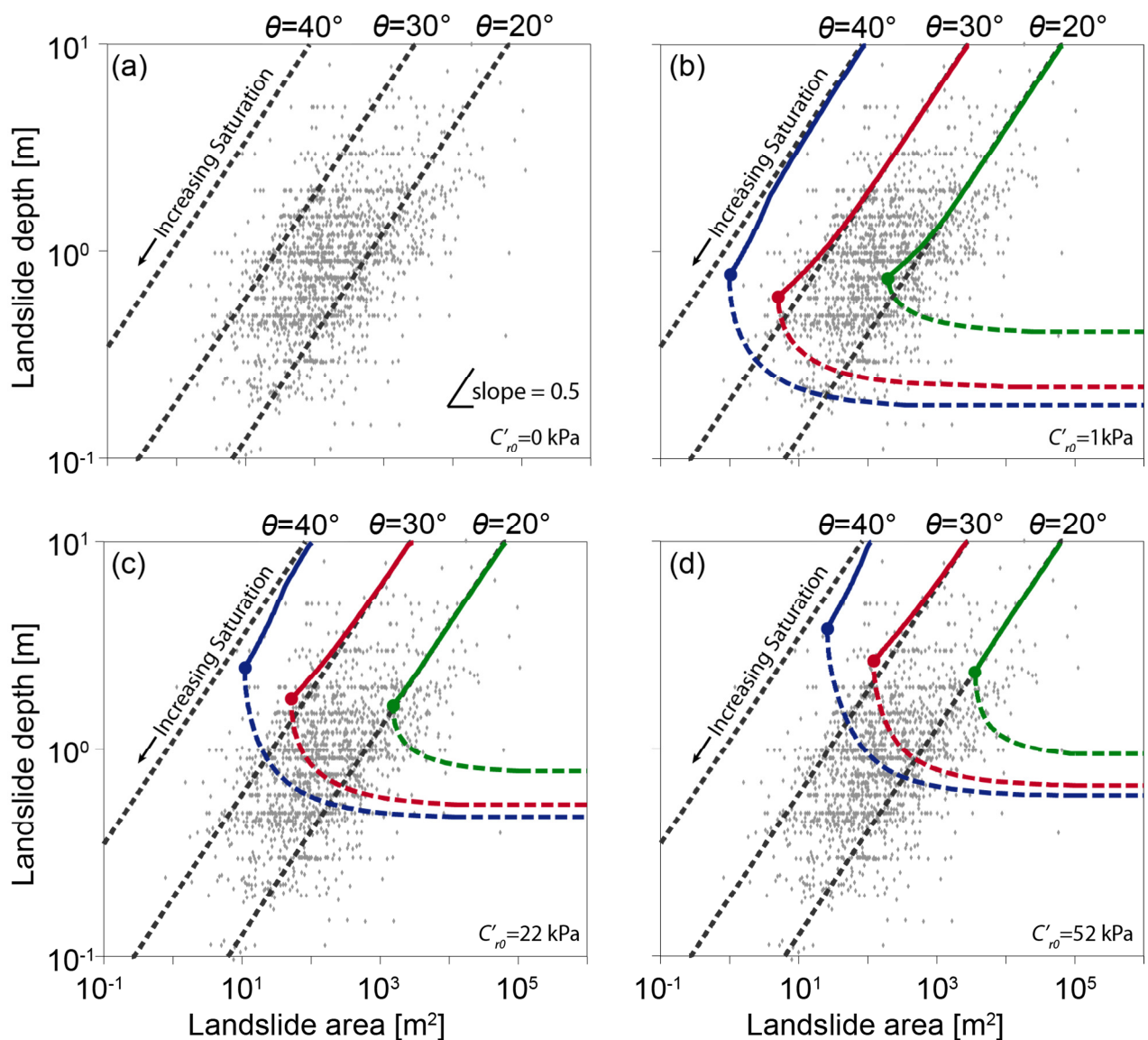

046

047
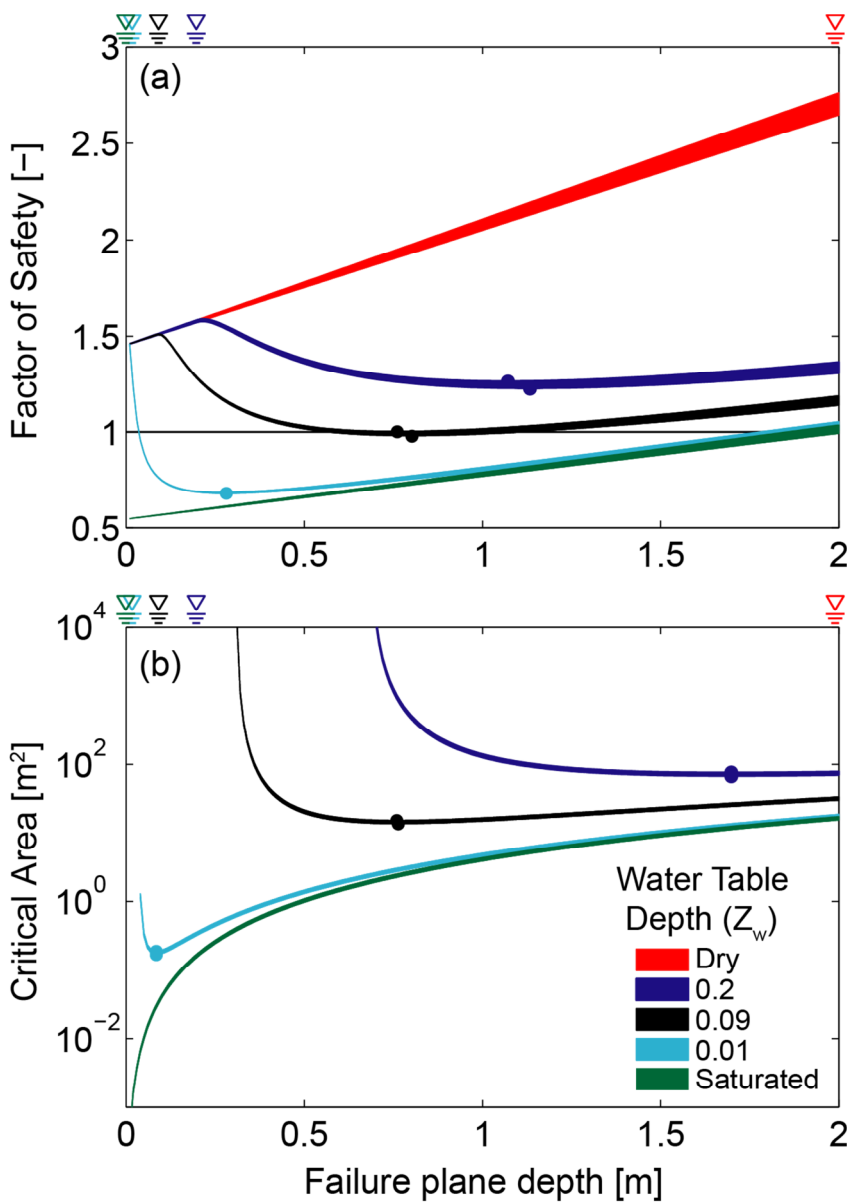
Figure 8: the factor of safety (a) and critical area (b) as a function of length-width (l/w) ratio for a block

of soil with θ=36°, ϕ=40°, and γ_s=15.7 kN m^{-3}, with a water table at the ground surface (i.e. fully saturated

soil) and where resistance is provided by: cohesion only (dashed lines) and both friction and cohesion (solid

lines). Dots indicate l/w ratios that minimize FS (a) and critical area (b) for each depth. In (a) the block area

is held constant at 60 m^2 (representative of the CB-1 scar) to calculate FS. In (b) the grey PDFs on the x and

right axes show l/w ratio and area distributions respectively for 19 landslides in the Coos Bay catchment

[Montgomery, 1991; Larsen et al., 2010]. The black rectangles between panels (a) and (b) are illustrative of

the l/w ratios corresponding to their x-axis location. Least stable shapes are equi-dimensional considering

only cohesion but longer than they are wide once friction is included.
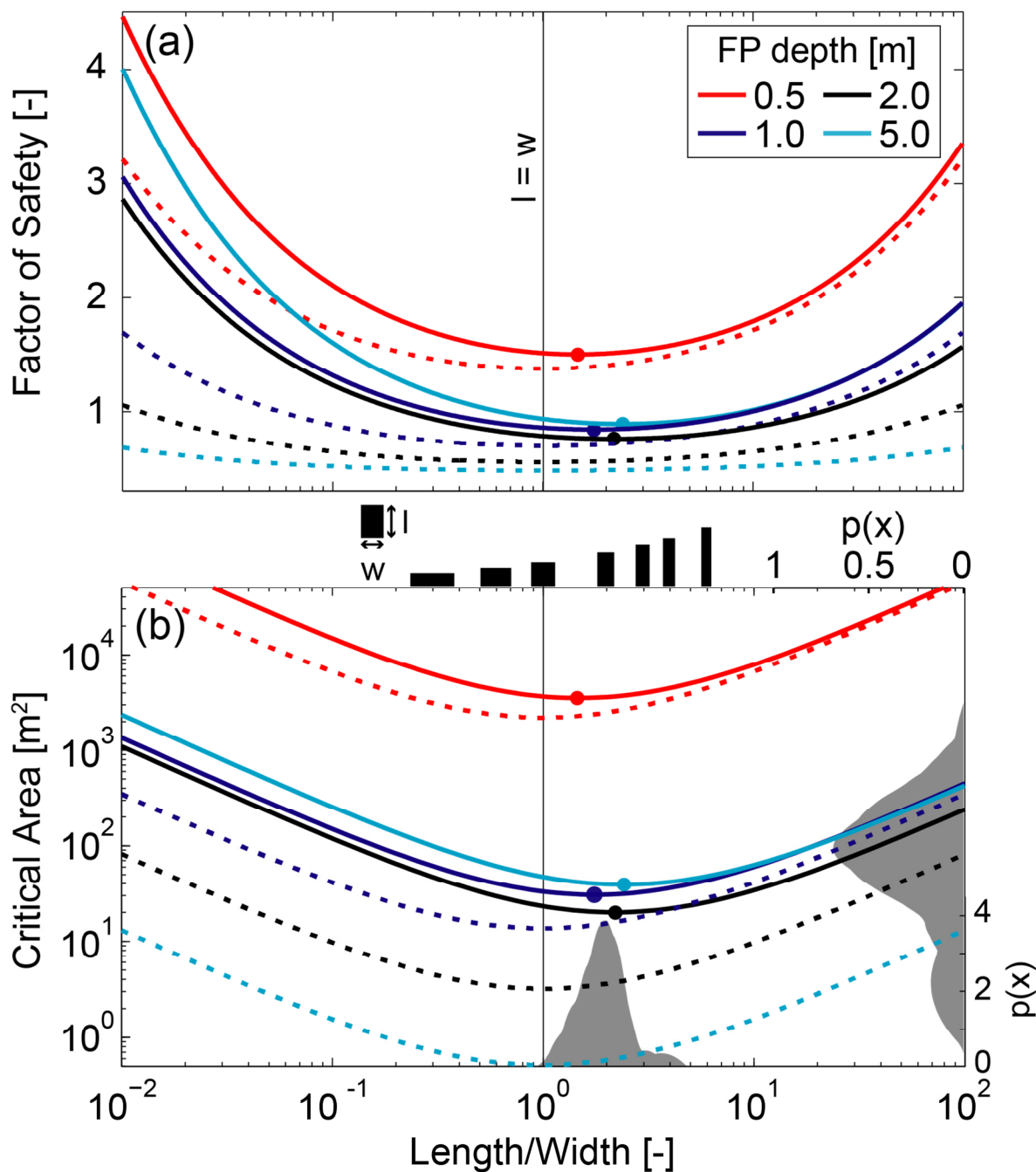
Figure 9: Black crosses show landslide scar depth and area for a global compilation of soil landslides

059   *[Larsen et al., 2010]. Colored lines show the modelled relationship between failure plane depth and critical*

060   *area for slopes with θ= 20°, 30° and 40°, ϕ'=40°, and γ$_s$=15.7 kN m^{-3}. Different panels reflect different root*

061   *cohesion scenarios: (a) C'$_{r0}$ = 0, (b) C '$_{r0}$ = 1, (c) C'$_{r0}$ = 22 (the CB-1 value), and (d) C'$_{r0}$ = 52 kPa*

062   *(representing old growth forest). In every case j=4.96 kPa^{-1}. Solid lines indicate the relationship between*

063   *critical depth and area when neither are constrained, with filled circles indicating where these are*

064   *minimized. Dashed lines represent the relationship for a saturated soil where depth is limited by soil*

065   *depth. The model predicts a theoretical lower limit to landslide area given depth, and the θ=40° curve is a*

066   *lower bound on the observed scar areas. When landslide depth becomes limited by soil depth, critical area*

067   *increases as depth decreases, creating a theoretical lower limit on landslide depth for a given critical*

068   *area.*

069